

NUS HIGH SCHOOL OF MATHEMATICS AND SCIENCE

SINGAPORE SPACE CHALLENGE 2009

SINGAPORE SPACE AND TECHNOLOGY ASSOCIATION

Avalon Satellite System

Authors:

NGUYEN Manh Huy
ONG Hao Yi
RAMAKRISHNAN Vijay
VO Thanh Minh Tue

Advisor:

WONG Chee Long

May 5, 2009

Abstract

Maritime surveillance such as piracy detection and rescue missions in the straits of Malacca is of fundamental importance to Singapore's economy and security. We propose a Spaceborne Polarimetric Interferometric Synthetic Aperture Radar (Pol-InSAR) system consisting of a pair of bi-static SAR configurations for maritime surveillance. The bi-static SAR configurations are based on a master satellite (active SAR transmitting satellite) and two passive SAR receiver microsattellites.

The master satellite consists of an active Phased Array Radar with Dual Polarimetric capabilities. The receiver-only microsattellites each have a passive dual polarized receiver antenna and are positioned 10km behind the master satellite in flying formation, allowing single-pass dual polarimetric SAR interferometry.

We have used a unique interferometric cartwheel for the trailing satellite flying formation that can image ship targets moving between 10 m/s to 50 m/s in real-time (from container vessels to speed boats), create digital elevation models and is capable of superresolution for detailed imagery. By innovatively coupling the properties of SAR interferometry with SAR polarimetry, our satellite system can give detailed 3D ship models of targets (based on texture, dielectric properties, geometry etc) so that ships, whether a fishing vessel or a pirate speed boat, can be accurately classified.

Our imagery system can work on three different modes, the Stripmap (high swath range), Spotlight (high resolution) and ScanSAR for flexible imagery capability depending on the scenario, whether it is scanning target ships over vast sea expanses or taking high resolution images of target ships for characterization. This shows a flexible approach to a vastly complex problem of ship imagery.

For ship tracking, we propose two dedicated communications antennas, one channel for the 406 MHz distress beacon and one channel for the AIS transponder information on ship coordinates and velocity. Our system combines AIS information with SAR imagery of the Strait, so that we can effectively sieve off legal, registered ships and target the rest for suspected piracy activities. We show that our satellite system is the best solution for ship tracking and classification with all-weather capability and sufficient ground coverage, making it a cost-effective alternative to other earth observation systems.

With a combined injected mass of 1070.46 kg, our mission lifetime is designed to be at least five years. The response time to an emergency beacon signal is at most 15.2 minutes and real-time imagery down-link is based on the Singapore Global Maritime Distress & Safety System (GMDSS) monitoring ground station. The total cost of design and maintenance is projected to be S\$286.6 million, meeting the competitions stringent standards.

Contents

1	Introduction	6
1.1	Introduction to the project	6
1.2	Ship tracking	6
1.3	Ship classification	6
1.4	Why is Polarimetric-Interferometry the best solution for ship classification?	8
1.5	Cross-track and along-track interferometry displayed by our flying formation	9
2	Imaging payload	11
2.1	Mission requirement	11
2.2	Imaging payload	11
2.2.a	Active Synthetic Aperture Radar transmitter	11
2.2.b	Selection of X-band SAR transmitter physical properties	11
2.2.c	Scanning and imaging configuration	13
2.3	Passive dual polarimetric SAR receiver (for trailing satellites)	14
2.4	Integration of SAR images	16
2.5	The Interferometric Cartwheel system	16
2.6	Conclusion	19
3	Tracking payload and methods	20
3.1	Tracking payload	20
3.2	Tracking method	20
4	Mission Design	22
4.1	Mission Requirements	22
4.2	Phase definition	22
4.3	Orbit maneuvering to final system formation	22
4.4	Functionality	24
4.5	Perturbations	24
4.6	Delta V Budget	24
4.7	Selection of launch vehicle	26
4.7.a	Launch vehicle selection	26
4.7.b	Weather considerations	26
4.7.c	Payload adaptor	26

5	System overview	27
5.1	Contingency	27
5.2	System overview	27
6	Propulsion	30
6.1	Introduction	30
6.2	Architecture trade studies	30
6.3	Hall effect thruster	30
7	ADCS and orbit control	32
7.1	Overview of spacecraft configuration options for the main satellite	32
7.2	ADCS requirement for the main satellite	32
7.3	Selection of spacecraft control type for the main satellite	32
7.4	Overview of spacecraft configuration options for trailing microsattellites	34
7.5	Selection of spacecraft control type for trailing satellite	34
7.6	Orbit Determination and Control	34
8	Communication subsystem	35
8.1	Objective	35
8.2	Frequency selection	35
8.3	Concept operation	36
8.4	Communication payload	36
8.4.a	Link budget calculation	36
8.4.b	Main satellite	36
8.4.c	Trailing satellites	36
8.4.d	Transmitter configuration for main satellite	38
8.4.e	Transmitter configuration for the trailing satellite	38
9	Command and data handling system	39
10	Power subsystem	42
10.1	Power requirements	42
10.1.a	Solar arrays	42
10.1.b	Primary batteries	42
10.1.c	Secondary batteries	44
10.2	Power distribution system	44
10.2.a	Architecture	44
10.2.b	Battery chargers	44
10.2.c	Converters	45
11	Thermal subsystem	46
11.1	Radiators	46
11.2	Louvers	46
11.3	Insulation	46
12	Cost analysis	47

13 Conclusion	49
A AIS Ship tracking	50
B Cospas-Sarsat emergency beacons	52
C A single SAR system	54
D Problems with a single SAR system	55
E Polarimetry	57
F SAR interferometry	59
G Polarimetric interferometry	63
H Applications and constraints of our unique flying formation	64
H.1 Digital Elevation Modeling	64
H.2 Superresolution	64
H.3 Moving object detection	65
I Imaging instrument trade-offs	66
I.1 High Resolution Optical Sensors	66
I.2 Hyperspectral sensors	66
I.3 Real aperture radar	66
I.4 Thermal infrared	66
I.5 Microwave remote sensing	67
I.6 Single SAR satellite consisting of both transmitter and receiver in repeat-pass mode	67
J Ship tracking using AIS and SAR imagery	68
K Propulsion trade study	69
L Hall effect thruster	70
M Attitude Sensors	71
M.1 Star sensor	71
M.2 Sun sensor	71
M.3 Rate gyros	71
M.4 Actuators	72
M.5 Engine gimbal	72
M.6 Antenna gimbal	72
N Hill equations	73
O Integration of SAR images	74

P	Operating area and spatial resolution calculations	75
P.1	Operating area	75
P.2	Spatial Resolution	76
Q	Power subsystem	78
Q.1	Eclipse time calculation	78
Q.2	Solar array sizing calculations	78
Q.2.a	Main satellite	78
Q.2.b	Trailing satellite	80
Q.3	Primary battery	80
Q.4	Secondary battery	81
R	Thermal subsystem	82
S	Antenna calculation	85
T	Optical/laser trade study	86
U	Deployment mechanism	88
U.1	Launch vehicle detachment	88
U.2	Solar array drive	88
U.3	Antenna	89
U.4	SAR (main satellite)	89
U.5	Cable antenna	89
V	Link budget	90

Chapter 1

Introduction

1.1 Introduction to the project

Maritime surveillance is an important application of many space based Earth observation systems. It is the key pillar to our mission objective and hence needs to be addressed with the highest priority while designing our satellite system. There are two main considerations that need to be met in order to perform maritime surveillance.

1.2 Ship tracking

First, the system must be capable of *ship tracking*. Ship tracking refers to the information of ship coordinates, velocity and intended route relayed by the satellite to the ground station for analysis.

For this purpose, our system uses two dedicated communications antenna channels: one for the 406 MHz distressed signal tracking transmitter beacon present in all licensed shipping vessels, which can be activated during an incident; and one for the increasingly popular AIS VHF transponder which relays GPS information about ship location, velocity and intended route to the ground station. With these two channels, all registered vessels in the Straits of Malacca are accounted for so that distress calls are immediately addressed for Search and Rescue operations and specialized ship tracking software can calculate collision avoidance paths efficiently.

However, the problem with solely relying on ship tracking is that 90% of all distress calls from emergency beacons are false alarms; and AIS transponders can be ‘tweaked,’ mistakenly or purposely, to reveal wrong information about the ship’s coordinates. This can lead to millions of dollars lost in Search and Rescue operations on false distress calls. Moreover, illegal ships which are not licensed, whether engaging in illegal fishing or pirate activities, cannot be tracked since they would most likely refuse to install AIS transponders for their tracking. This is the main weakness of most tracking-based satellite systems and motivates us to study ship classification for further improvement.

1.3 Ship classification

To address the issues stated in the previous section, the system must be capable of *ship classification*. Ship classification refers to the identification of the physical property of a ship, like its size, shape and material properties, so that identification (e.g. oil tanker, fishing boat) can take

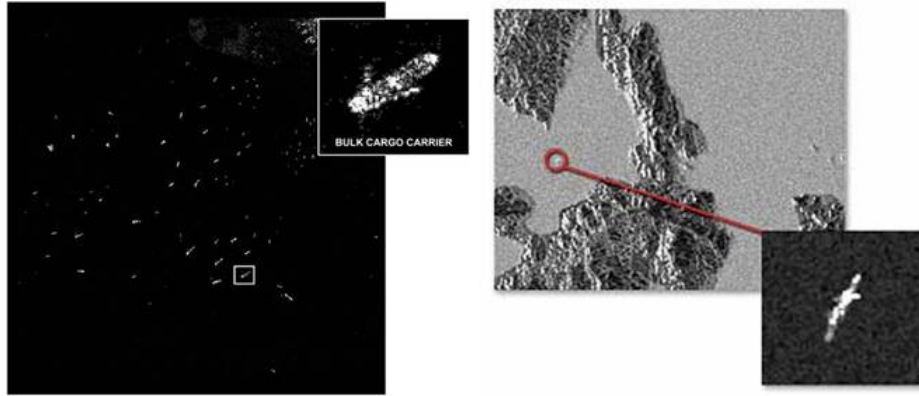


Figure 1: Greater ship contrast using HH polarization (left) than no polarization (right)

place. Ship classification was beyond the scope of radar imaging until techniques like Polarimetric-Interferometric Synthetic Aperture Radar (Pol-InSAR) imagery, ship scattering matrix databases and Vessel Classification Algorithms were recently designed.

Our system employs the Polarimetric-Interferometric Synthetic Aperture Radar (Pol-InSAR) imaging technique to image and classify different types of ships in the straits of Malacca. Here, our imaging payload consists of a main dual polarized phased array SAR transmitter antenna in the transmitting satellite and two passive SAR receivers, also dual polarized, on each trailing satellite. The two trailing satellites are in an interferometric cartwheel flying formation with the main satellite. Because they are smaller than the main satellites, they are also called *microsatellites*.

The SAR-based imagery system has many advantages, particularly all-weather and all-lighting capabilities. Because Singapore is in the tropics and cloud cover is evident, an SAR based system should be used. An extensive trade study of different sensors is presented in Appendix I. SAR radars alone can scan wide swaths and spot small targets quickly, perfect for ship detection. Very briefly, ship detection using SAR alone relies purely on the intensity of the backscattered radar waves. Because the material of a ship surface is rougher than that of the sea surface, resulting in greater diffuse reflection, more energy of the transmitted wave is received by the satellite system. Hence, the target ship will be brighter than the sea in a typical SAR image. However, during rough seas, spotting ships becomes a great problem.

To complement the advantage of scanning over wide swath area of SAR, we use polarimetry to enhance image resolution because the backscatter of transmitted polarized EM waves from a ship carries vital information about textural fine-structure, target orientation and shape, symmetries (reflectivity) and material constituents (dielectric properties) that an ‘amplitude-only’ SAR system would not give. Therefore, even during rough sea conditions, it is very easy to spot a ship from the sea using radar polarimetry because the inherent back-scattering properties of the ship and the sea are different. Moreover, polarimetry enhances the contrast between the ship and sea for better detection. X-band imagery in HH polarization is preferred for detecting a ship because the ship-sea contrast is higher for HH polarizations due to the increased scatter at VV by the surface capillary waves. This results in lower background clutter at HH polarization (see Figure 1). Note: HH means transmit with horizontal polarization and receive with horizontal polarization.

However, ship classification using radar polarimetry by itself cannot occur because the image

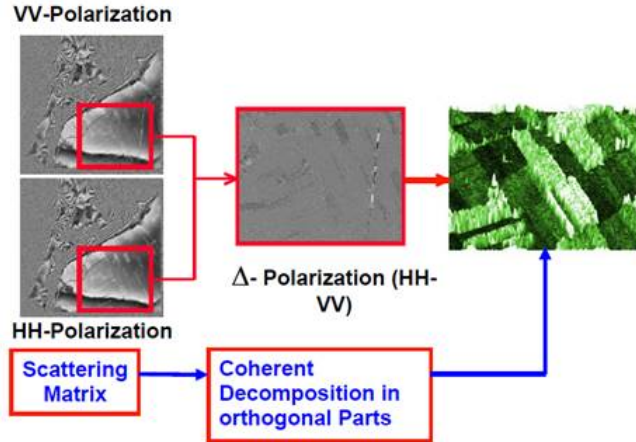


Figure 2: The integration of two images taken using polarimetry to form 3D POLIN-DEM images (Keydel [32])

geometry (the ship geometry) is not very well defined using a single polarimetric system. The finer scattering structures of complex targets like ships needed for ship characterization can only be discerned if the height accuracy of the target is within 1 m^2 , according to Keydel [32]. This accuracy cannot be reached with a conventional Polarimetric SAR system.

More information on ship classification is presented in Appendices C and E.

1.4 Why is Polarimetric-Interferometry the best solution for ship classification?

The height accuracy of 1 m^2 can only be reached by combining the property of SAR polarimetry with SAR Interferometry [32]. Interferometry is the use of the phase difference of two received radar echoes of a single target at different positions to calculate height information about the target. In our single-pass system consisting of two receiver-only trailing satellites in flying formation, it is possible to recover co-registered textural properties (from polarimetry) and spatial properties (from interferometry) simultaneously. The fly formation is chosen to maximally utilize phase information while reducing costs and complexities on a single satellite. This allows the extraction of Digital Elevation Maps (DEM) from Interferometric SAR image data with the additional benefit of obtaining co-registered three-dimensional ‘POLIN-DEM’ information (see Figure 2). Detailed description about Polar Interferometry is documented in Appendix G.

For ship classification, this POLIN-DEM 3D information (which includes the scattering properties of points in a complex target where the relative height between any of the two points needs to be accurate) can be compared to an existing database of scattering models of vessels (e.g. the Vessel Classification Algorithm (VCA), DECLIMS and so on) to classify the ship into different categories (Margarit and Mallorqui [38]). See Figure 3.

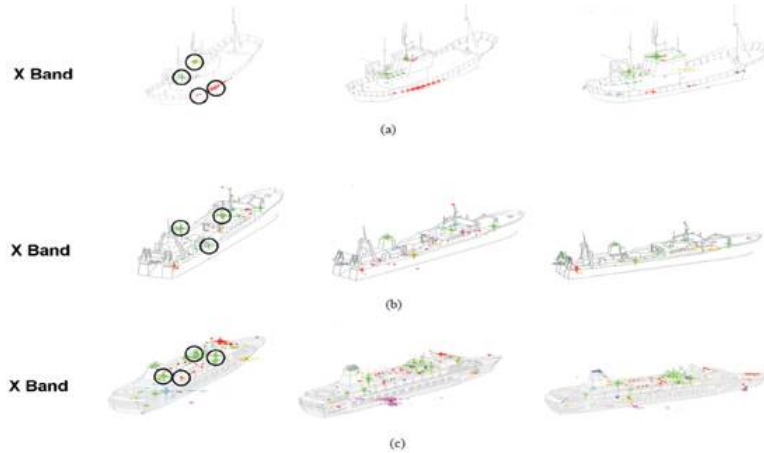


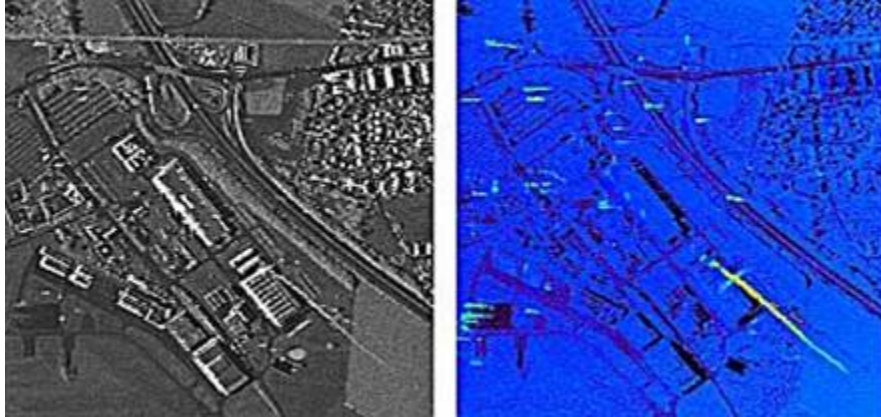
Figure 3: Three scattering geometries of ships: a) a Spanish fishing vessel 30 m long and 7 m wide, b) an Icelandic fishing vessel 70 m long and 15 m wide, c) a passenger ferry 200 m long and 30 m wide at varying incidence angles to the transmitting satellite. These geometries are recognized by the Vessel Classification Algorithm to classify a ship according to its polarimetry backscatter measured accurately using interferometric SAR for geometry. (Margarit and Mallorqui [38])

1.5 Cross-track and along-track interferometry displayed by our flying formation

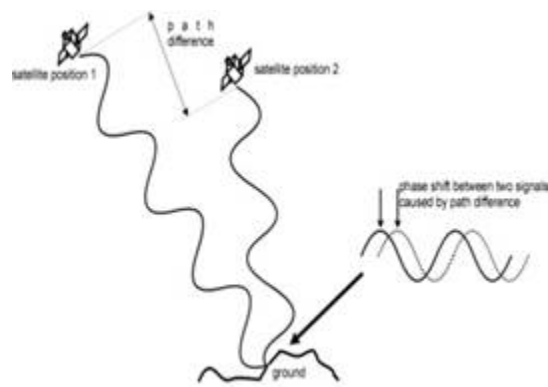
We choose a single-pass interferometry system, consisting of a single transmitting satellite and two receiver trailing satellites. Because our ship targets are not stationary over time, a conventional repeat-pass mode will cause a lot of error in the phase difference calculated of the moving target (Peterson [45]).

We used a unique interferometric cartwheel flying formation with specific parameters calculated for the two trailing satellites to prevent temporal decorrelation and simultaneously detect moving ships accurately at speeds of within 5 m/s to 50 m/s depending on baseline length calculated. This is yet another form of ship tracking because the phase difference collected by the two trailing satellites will accurately detect moving targets with respect to the stationary background. Moreover, it clearly meets our mission requirement of tracking speed boats that more often cannot be imaged by conventional imagery systems. Using our flying formation, we can accurately detect the velocity of the moving target, and this property becomes prominent during rough seas when SAR imagery is not very accurate.

We can switch to along-track interferometry to map targets based on their velocities (see Figure 4). This is extremely helpful in detecting pirate speed boats. Detailed information on our fly formation is presented in Appendices F and H.



(a) Full azimuth bandwidth E-SAR image in X-band (left) and corresponding along-track interferometric phase. Blue color corresponds to zero phase and represents the stationary targets. The moving targets are shown in green, yellow and orange depending on their velocity.



(b) Basic principal of interferometry displayed by our flying formation trailing satellites

Figure 4: Interferometry

Chapter 2

Imaging payload

2.1 Mission requirement

The specific objectives are:

- 1) Detection of moving ships in the strait.
- 2) Detection of fast moving small pirate vessels.
- 3) Environmental monitoring, like oil spill detections.

As introduced in chapter 1, our payloads are chosen to fulfill the design of a Polarimetric InSAR system. The choices of payload will affect the overall system complexity and capacity. Hence we have done extensive researches on SAR payload.

2.2 Imaging payload

The imaging payload for our system consists of a *Dual Polarized Synthetic Aperture Radar (SAR) transmitter* for the main satellite and a *Dual Polarized Synthetic Aperture Radar (SAR) receiver* for the two receiving trailing satellites.

2.2.a Active Synthetic Aperture Radar transmitter

Our satellite transmitter system features an advanced high-resolution X-Band Synthetic Aperture Radar instrument based on the Active Phased Array Technology, which allows the operation in Spotlight, Stripmap and ScanSAR Mode with various polarizations. It has the electronic beam forming flexibility of the active phased array that is capable of acquiring high resolution images for detailed analysis and wide swath imaging for detection purposes. See Figure 6 and Table 1.

2.2.b Selection of X-band SAR transmitter physical properties

First, we chose the X-band for the transmitting frequency with 9.65 GHz. According to our simulations with STK, we found that the X-band transmitter had a much greater operating area for the satellite (1000 km radius) than the Ku-band, L-band and C-band due to higher atmospheric attenuation (see Figure 12). Moreover, the resolutions for both along track interferometry and

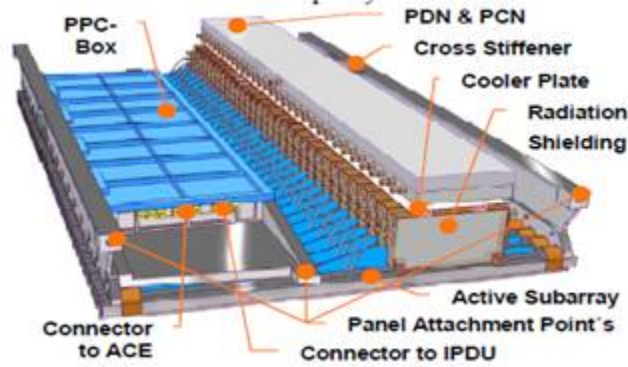


Figure 5: The rear view of our recommended phased array radar [from the Boeing Company]

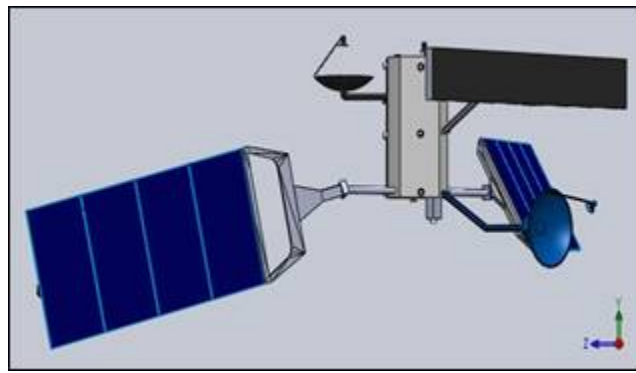


Figure 6: The Phased Array Radar incorporated in our satellite model

Antenna Aperture size	4.8 m × 0.7 m
Operating area	2000 km [diameter]
Wavelength	3.1 cm
Bandwidth	30 MHz
Transmitting power	2200 W
Instrument Average power	406 W
Instrument Peak power	3863 W
Pulse repetition frequency	3000 Hz to 6500 Hz
Receiver gain	30 dB
S/N ratio	-12.5 dB
Noise bandwidth	4.5 dB
Mass	109.23 kg
Data rate	120 Mbps
Center Frequency	9.65 GHz
Incidence Angle Range	15 deg to 60 deg
Mass	235 kg

Table 1: Physical parameters of the SAR transmitter [from Boeing]

	Single Pol	Dual Pol
Polarizations	HH or VV	HH/VV, HH/HV or VV/VH
Scene Dimension	500 km \times 300 km	250 km \times 150 km
Predicted performance range (from manufacturer)	20° to 45°	20° to 45°
Azimuth Resolution	33 m	66 m
Ground range resolution	17 m to 34 m (depending on radar inclination)	17 m to 34 m

Table 2: Resolution of strip map mode according to our calculation

DEMs were lower in X-band than the rest. This satisfies the mission objective of tracking the vast 400 nautical miles area of the straits of Malacca with high resolution imagery.

With the X-band frequency, the radar aperture size was set to 4.8×0.7 m with a total area of 3.6 m^2 . At a swath width of 100 km, the relationship between antenna size, swath width, and azimuth resolution requires the radar area to be above 2.2 m^2 . With a 3.6 m^2 area, we get an acceptable azimuth resolution of 4.7 m with a not a very high requirement of transmitting power because as the radar array panel decreases, the transmitting power increases. The transmitting power is 2200 W for an operating area of 1000 km operating radius.

2.2.c Scanning and imaging configuration

The payload is capable of Multi-Scenario Imagery, primarily because of the advanced Phased Array Radar that can be electronically steered to generate different radar tracking patterns depending on the scenario. The modes of imagery are the Strip Map mode, the SpotLight mode and the ScanSAR mode. All of these modes have been demonstrated successfully in our STK simulation.

The Strip map mode

The ground swath is illuminated with continuous sequence of pulses while the antenna beam is fixed in elevation and azimuth. This results in an image strip with a continuous image quality in the flight direction. See Table 2.

The Spotlight or High resolution spotlight modes

Two variants of the spotlight mode (Spotlight SL) and High Resolution (Spotlight HS) are designed with different values for azimuth resolution and scene size (see Table 3). SL and HS modes use electrical beam steering in azimuth direction in order to increase the illumination time i.e. the size of the synthetic aperture. The larger aperture results in a higher azimuth resolution at the cost of azimuth scene size. The electronic beam steering is done by our Phased Array Radar that uses an onboard computer algorithm to coordinate the wavelets from each array of the radar. Note: Electronic beam steering does not physically steer the SAR radar; it electronically adjusts the arrays in the radar to change patterns.

	Single Pol	Dual Pol
Polarizations	HH or VV	HH/VV
Scene Dimension	10 km × 10 km (SL) 10 km × 5 km (HS)	10 km × 10 km (SL) 10 km × 5 km (HS)
Predicted performance range (from manufacturer)	20° to 55°	20° to 55°
Azimuth Resolution	1.7 m (SL) 1.1 m (HS)	3.4 m (SL) 2.2 m (HS)
Ground range resolution	1.48 m to 3.49 m	1.70 m to 3.49 m

Table 3: Resolution of spotlight mode according to our calculation

	Single Pol
Polarizations	HH or VV
Scene Dimension	500 km × 200 km
Predicted performance range (from manufacturer)	20° to 45°
Azimuth Resolution	18.5 km
Ground range resolution	1.70 m to 3.49 m

Table 4: Resolution of scanSAR mode [derived from the SAR parameters]

The ScanSAR mode

The ScanSAR imaging mode (Table 4) combines the ability to acquire high resolution images for detailed analysis with wide swath imaging for overview applications. The electronic antenna elevation steering is used to switch after bursts of pulses between swathes with different incidence angles. Due to the switching between the beams only bursts of SAR echoes are received, resulting in a reduced azimuth resolution. But the swath width is high, at around 100 km range for wide scanning.

2.3 Passive dual polarimetric SAR receiver (for trailing satellites)

The passive SAR receivers (see Table 5) are used to detect the radar echoes of the transmitting satellite so that information of varying amplitudes of the returning echo, position of target, phase of incoming signal and polarity can be acquired.

As shown in Figure 7, the echoes are taken by the antenna and processed through the RF receiver and F1 sub system. We use a low noise amplifier (LNA) in the F1 subsystem to amplify the RF signal. This information is stored in a 20 Gbit memory drive and compressed. The information is passed to the radar control unit and transferred to the earth stations by X-band telemetry. See Figures 8 and 9.

The typical orbit scenario for the Trailing satellite is as follows:

- (1) 2 minutes to 3 minutes are dedicated to image acquisition.

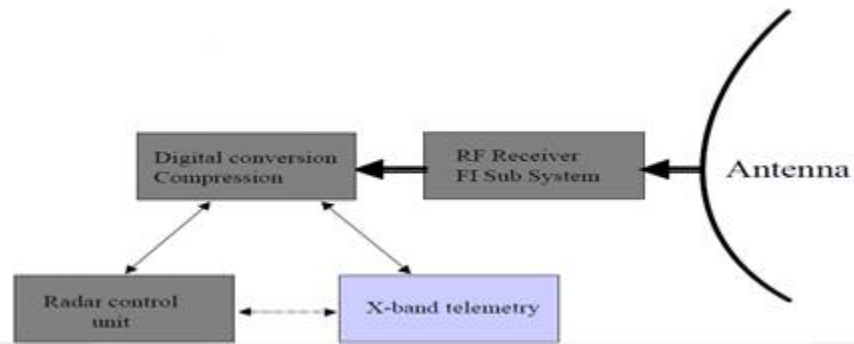


Figure 7: Image payload transfer design of the trailing satellite [Adapted from CNES microsatellite subsystem]

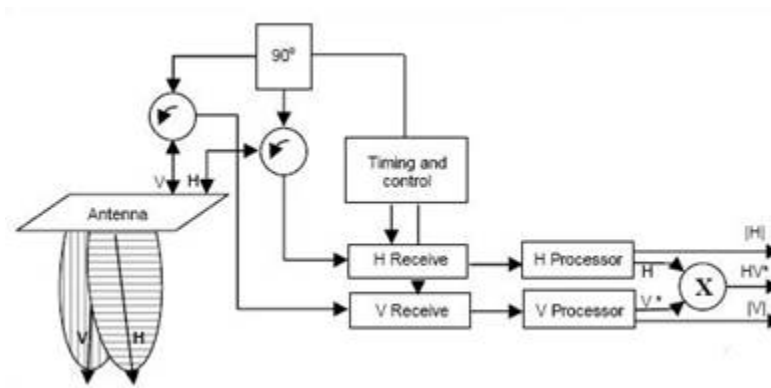


Figure 8: Circuitry of SAR antenna receiver adapted from LRO's dual polar dish antenna. The receiver can be switched to H or V depending on the image needed. This greatly enhances the flexibility of our system as it can receive both types of polarization.

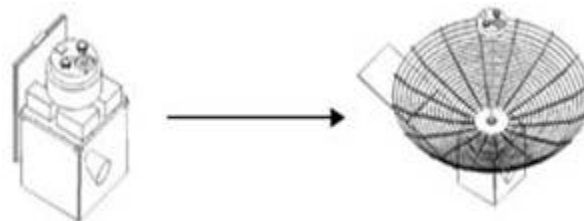


Figure 9: Due to budget limitations, space availability in the launch vehicle and mass considerations, we decided to use a deployable dish-type antenna for the receiver payload. We consider the deployable concept of the 'WRAP-RIB' designed by Lockheed Martin

Antenna receiver size	2.4 m diameter	
Mast length	1.2 m	
Antenna Gain (RF loss included)	26 dBi (very approximate estimate)	
Instrument Data rate	160 Mb/s	
Memory Size	20 Gbits	
Telemetry Size	Up to 50 mbps	
Consumption	Imaging mode	50 W
	Telemetry mode	50 W
	Stand-by mode	20 W
Mission Lifetime	5 years	

Table 5: Physical parameters of the SAR receiver [from Boeing]

- (2) Images are stored in a 20 Gbit memory.
- (3) 8 minutes to 10 minutes are dedicated to telemetry through an X-Band channel (developed for the DEMETER mission).
- (4) Stand-by mode (solar pointing of the SA) is set for the remaining part of the orbit.

The trailing satellite is connected to the main satellite via a K-band intersatellite antenna. Information from the ground station is relayed from the main transmitting satellite to the trailing satellites.

2.4 Integration of SAR images

The integration of two SAR images to form the DEM is a very complex process and beyond the scope of this design document. The flow chart in Figure 10 summarizes the basic steps. Appendix O gives some insight into this.

2.5 The Interferometric Cartwheel system

The *Interferometric Cartwheel* is a special satellite configuration for SAR interferometry, which was originally proposed by French scientists [Center National D’Etudes Spatiale]. From our trade study, this formation was chosen because it can meet Pol-InSAR requirements while simplifies the complexity of InSAR imaging. Formation flying is also a trend of modern satellite designs and many countries such as the US, China and India are pursuing their own formation-flying systems. Ours consists of two trailing satellites with SAR receivers that follow a master satellite with a conventional SAR in such a way that one trailing satellite appears to rotate around the other and provide sufficient baselines for along-track and cross-track interferometry throughout the whole orbit.

Receiver spacecraft performing single-pass interferometry receive the same signal with a small time offset. This eliminates the problem of changing terrain dynamics between repeat passes distorting the resulting elevation models. It is especially important for our mission to map speed boats because ships and boats are constantly moving in the sea and this motion is mapped much better using a single-pass than a repeat-pass, which convention SAR systems used.

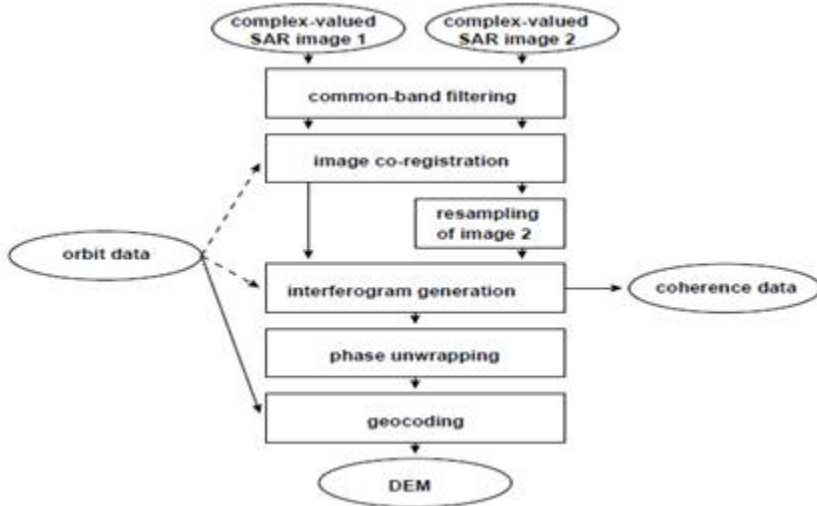


Figure 10: Interferometric cartwheel configuration of two trailing microsattellites and one transmitting satellite

The spatial separation of the receivers also determines the nature of the data products and their applications. Cross-track baselines are used to generate terrain elevation data while along-track baselines are used to map motion in the resulting images. Note: the baseline distance refers to the distance between the two microsattellites.

$$B_{\text{crit-c}} = \frac{2B_{\text{rg}}\lambda R \tan(\theta - \nu)}{c} \quad (2.1)$$

$$B_{\text{crit-min}} = \frac{\lambda R \sin(\theta)\delta\phi}{2\pi\delta h} \quad (2.2)$$

Above are the formulas for the critical and minimum baselines from Peterson [45].

The critical baseline in Eq. (2.1) depends on the signal bandwidth B_{rg} , the wavelength, the range, the incidence angle, the local slope of the imaged terrain and the speed of light c . The minimum baseline in Eq. (2.2) is determined by the wavelength, the range, the incidence angle, the interferometric phase error, and the maximum allowable height error in the elevation measurement h . We kept the maximum allowable height error to be 1 m² for Polarimetric fine-scattering generation (discussed in chapter 1). The incidence angle was varied from 15° to 60°. The range was determined from the altitude of the satellite (600 km). See Figures 11 and 12.

According to our calculations, the critical cross-track baseline should be 6.2 km for acquiring DEMs without signal decorrelation. Our complete calculations are presented in Appendix H. Accordingly, we found the eccentricity to be 0.0066 for the second trailing satellite using the numerical approach in STK 8.0 for these baseline variations.

A complete set of formulas for operating area and spatial resolutions that we used is presented in Appendices H and P.

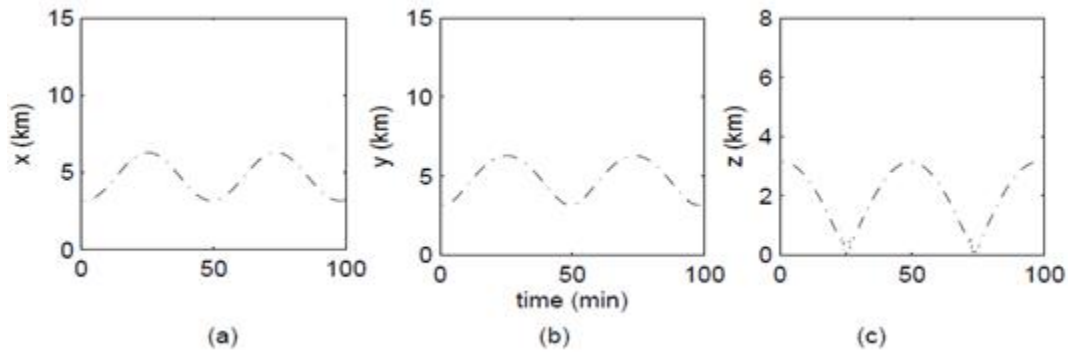


Figure 11: Interferometric cartwheel available baseline distances between the two trailing satellites in the (a) cross-track direction, (b) along-track direction, and (c) vertical direction. Variations in the argument of perigee and eccentricity cause the cross-track and along-track coupled baselines to both vary between the critical baseline and one-half the critical baseline for each transmit band; and the vertical baseline to vary between zero and one-half the critical baseline. Our graphs have been carried out and verified using STK software.

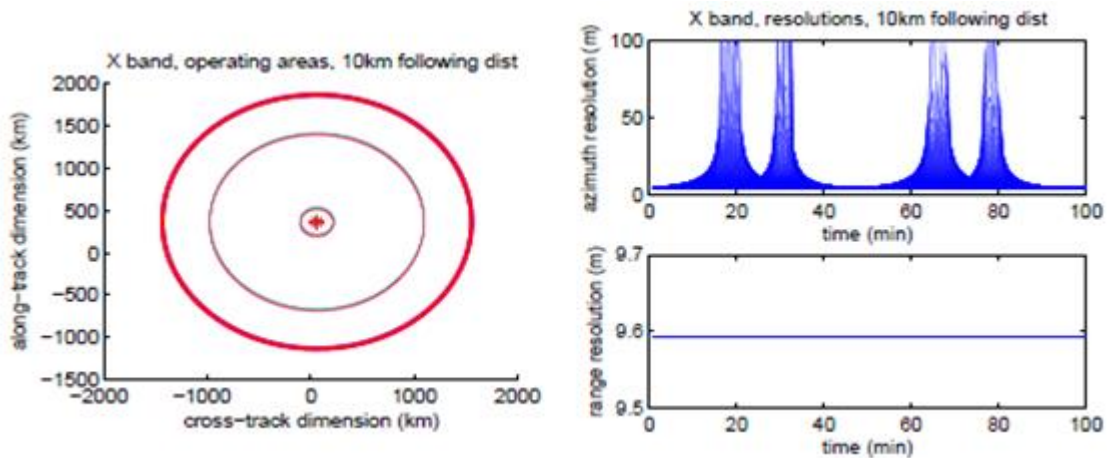


Figure 12: Left: operating area of the bi-static pair (the thin red line for incidence angle from 15° to 60° which we proposed and the thick line is the theoretical maximum). Right: resolution for the bi-static pair for along-track and cross-track directions as calculated by STK 8.0. The right graph is the worst case resolutions of the InSAR formation at the edge of the operating area but towards the center of the operating area, we can switch to polarimetric imagery to much better resolution, but swath width would be compromised if so.

2.6 Conclusion

We have carried out *extensive* trade studies and concluded that a formation flying SAR system is the most suitable for our purposes within the given constraints. An active SAR transmitter and passive SAR receiver have been selected as the primary payloads for the transmitting and receiving satellites, respectively, for imagery. A 406 MHz distress signal receiver and AIS receiver have been selected as the secondary payload for tracking in this mission. These instruments are able to meet all three broad requirements of cooperative ship detection, pirate detection and environmental monitoring.

Chapter 3

Tracking payload and methods

3.1 Tracking payload

The 406 MHz distress signal receiver is described in Table 6.

Using the beamwidth (17.64°) and satellite system orbit period (51.43 mins), we calculated that the maximum possible distress signal pick-up time lag is 15.2 mins (assuming the beacon is activated just as the satellite passes by the region). This is well in the range of the 20 min competition requirement.

3.2 Tracking method

We use an innovative tracking method, taking advantage of both the AIS receiver and the SAR imagery system to track pirate and illegal vessels. First, the *SAR imagery* instrument is used to take a complete image of all the ships in Straits of Malacca. Preferably, this would be done in Stripmap mode or scanSAR mode, for greater swath width, so that the entire region is covered. Next, the imagery information from the SAR transmitter is transferred to the ground station, where it is matched with information of the AIS coordinates of the ship, also relayed by the satellite system. Next, the coordinates of the ship and its image are mapped onto each other.

To spot a pirate vessel, we can simply filter out the ships with correct coordinates (confirmed by both the AIS and imagery), and AIS information and isolate the ships that are illegally present in the region (without AIS licenses or very near large container ships). Finally, we can use the spotlight mode of the SAR imagery to take high resolution pictures of the suspect vessels, and use the SAR along-track interferometry to accurately map its velocity.

Based on the collected data, the ground station can use motion predicting algorithms (from Suchandt et al. [52]) to map a vessel's course and polarimetric value to model information about the vessel's characterization. Hence, information about the ship, such as whether it is a fishing vessel, inflatable

Type	Frequency-band	Gain	Halfpower Beamwidth	Mass	Diameter	Quantity
Parabolic Antenna	406 MHz	16 dBi	25.89°	5.8 kg	1.5 m	1

Table 6: Distress signal receiver specifications

Frequency	161.975 MHz
Data rate	2 Mbps
Operational temperature	-40 °C to 85 °C
Instrument power	0.18 W
Instrument mass antenna	51 g
Electronics	40 g
Antenna stowed	0.053 m × 0.053 m × 0.013 m
Antenna deployed	1.46 m × 0.013 m
Electronics	0.085 m × 0.085 m × 0.008 m

Table 7: AIS receiver specifications

boat or cruise liner, can be obtained (see Appendix J). The same principle applies to the distress signals of the emergency beacons. Once coordinates are spotted, the satellite system can zero in on the coordinates using the spotlight mode to take pictures of the scene, whether it is an accident or pirate attack, and relay the information to the ground station. Moreover, such imagery can be taken day and night in all weather conditions.

Chapter 4

Mission Design

This section will detail the determination of final orbit characteristics and the selection of the launch vehicle. As described in previous chapters, the complexity of a formation flying system requires us to carefully design the delta V budget.

4.1 Mission Requirements

Our orbital design is primarily intended for the tracking of ship activity in the straits of Malacca and the detection of potential distress signals, hence the need for optimum real-time coverage.

4.2 Phase definition

The mission is divided into 8 phases, outlined in Table 8.

4.3 Orbit maneuvering to final system formation

The exact mechanism for the maneuver is shown in our STK simulation. Once the three satellite payload is released from the launch vehicle, the two microsatellite receivers will fire their thrusters into an eccentric circular orbit. The eccentric orbit intersects the circular orbit of the transmitter satellite at one other point. However, by the time the two microsatellites reach that point, the transmitter satellite would be ahead of the microsatellites by a 10 km distance. (For this, we place the two microsatellites at a critically inclined orbit of $e = 0.092$ while the main transmitting satellite is placed in a perfect, circular orbit.)

The second maneuver requires the second microsatellite to fire its thrusters until its eccentricity is 0.0066 with a circular orbit. From here, the two microsatellites travel in an interferometric cartwheel formation, with the transmitting satellite leading the receivers. We adjusted the eccentricity of the first orbital maneuver such that the intersection of the orbital planes occurs when the transmitting satellite is 10 km leading the microsatellite flying formation.

Phase	Description
1) Launch	<ul style="list-style-type: none"> • Time from the instance power cord is severed prior to launch to satellites separating from the vehicle fairings. • Power provided by the primary batteries in the satellites
2) Orbital Insertion	<ul style="list-style-type: none"> • Time for the satellites to correct any launch injection errors and place themselves in the final mission orbits. • Solar arrays are deployed here and fully prepared to produce power for all the satellites.
3) Data Collection and Transfer	<ul style="list-style-type: none"> • When over the Straits of Malacca, data collection and transfer will occur simultaneously. • The SAR antenna is on and transmitting at a frequency of 9 GHz • Microsatellites have their RF receivers on, receiving the radar echoes of the transmitter, and data is stored in the 20 GBit drive and compressed. • The data transferred from the microsatellites to the transmitting satellite, via a K Band antenna • Info relayed the back to ground station via high gain antenna in main satellite.
4) Day Time, Silent Mode	<ul style="list-style-type: none"> • Once past the Straits of Malacca, the satellites are in ‘silent mode’, the primary ongoing process is charging of the batteries.
5) Eclipse, Data Collection and Transfer	<ul style="list-style-type: none"> • The satellites are in eclipse when it is behind the Earth and no longer in view of the Sun. • Data collection and transfer is the primary ongoing process to the ground stations. If the satellites are over the Straits of Malacca in the night time, they can continue to image the region for ship tracking.
6) Eclipse, Silent Mode	<ul style="list-style-type: none"> • Data collection and transfer does not occur here. Batteries are being recharged.
7) De-orbit Maneuvers	<ul style="list-style-type: none"> • This phase de-orbits the spacecraft so it will not pose a threat to future spacecraft.
8) Emergency mode	<ul style="list-style-type: none"> • Accounts for the emergency situation where the spacecraft tumbles out of control during an eclipse, should the satellite encounter a major anomaly. Calculations relating to this phase provide the most severe conditions in which each subsystem must operate. This way, the lifetime of the spacecraft is better preserved.

Table 8: Description of the phases in our satellite mission

	Main satellite	Microsatellite 1	Microsatellite 2
Semi-major axis (km)	6978.137	6978.137	6978.137
Eccentricity	0	0	0.000 46
Inclination (°)	0	90	90
Argument of perigee (°)	0	0	180
Right ascension (°)	0.012	0	0
True anomaly (°)	0	0	180

Table 9: Orbital elements of our satellite system calculated from numerical method for the Hill’s equation.

4.4 Functionality

Orbit calculations: The relative motions of a formation flying system are based on Hill’s equations, a set of differential equations. In our project, we use numerical methods to approximate the solutions (from Chen et al. [7]) and use STK to validate the results. They are shown in Table 9.

During an average 24-hour period, the satellite system makes 28 passes over Singapore. We used STK with a SAR sensor for the transmitting satellite with incidence angle ranges from 15° to 60° to compute the coverage time over Singapore.

Minutes of coverage in an average 24-hour period	= 99.54 minutes of continuous coverage
Maximum coverage duration for a single visit over Singapore	= 3.70 minutes
Minimum coverage duration for a single visit over Singapore	= 3.45 minutes
Period of Satellite	= 51.43 minutes

The calculations of the orbital elements are discussed in Appendix N.

4.5 Perturbations

Perturbations and drags are prominent disturbances affecting satellites in LEO. Perturbations are the result of assumptions made in equations, such as the Earth being a perfect sphere. There are also third-body perturbations, which have relatively small but significant effects on the satellite orbit. The sources of these are primarily the Moon and the Sun because the n -body problem is not addressed in calculations involving the satellite’s orbit around the Earth. There is also a ‘J2’ perturbation which addresses the precession of the satellite in its orbit due to the non-uniformity of the surface of the Earth.

At an altitude of 600 km, the amount of atmospheric drag is also great and the satellite thrusters need to be fired to correct their orbital paths. We used STK 8.0’s ‘J2 perturbation propagator’ and ‘Jacchia Atmosphere Model’ to simulate the perturbations involved. All the calculations are based on these two constraints.

4.6 Delta V Budget

The ΔV budget is broken up into 3 parts as shown in Table 10. All ΔV calculations were performed with the STARMAD software using Princeton university’s codes for orbital maneuvers.

Phase	Description	Main Trans- mitting satellite (m/s)	Trailing passive microsatellites (m/s)
Orbit Insertion Maneuver	Orbital insertion maneuvers, where the satellites correct for launch injection errors and place themselves in the final mission orbit. This section of ΔV also accounts for any maneuvers required should the total injected mass of the spacecraft exceed the launch vehicle's capacity.	0 (direct injection by launch vehicle)	2.78×10^{-3} (Microsat 1)* 2.792×10^{-3} (Microsat 2)*
Orbit Maintenance	ΔV is budgeted to counter atmospheric drag and other perturbations. The change in satellite velocity is calculated (Larson and Wertz [36]) and multiplied by the mission lifetime. This provides the total ΔV required for the operational duration of the satellites. (Phases 3 to 6).	$7.2 \times 5 = 36$	$5.2 \times 5 = 26$ (microsat1) 26 (microsat2)
De-orbit Maintenance	The ΔV budgeted for this must be accommodated so as not to contribute to the accumulation of space debris, and to ensure the safety of other spacecraft in the proximity. This maneuver is calculated by reducing the spacecraft's perigee to 30 km above the Earth's surface. The spacecraft will be unable to pull out from such an altitude and will proceed to burn up upon reentry (Phase 7).	0.04284	4.11×10^{-3} (microsat1) 4.11×10^{-3} (microsat2)

Table 10: Delta V budget components

*The two receiving satellites would first have to have a following distance of 10 km from the transmitting satellite. Second, the 2nd microsatellite must change its orbit from circular to circular eccentric with $e = 0.0066$.

4.7 Selection of launch vehicle

4.7.a Launch vehicle selection

The launch vehicle must meet the orbital requirements and be cost-effective. The Soyuz is chosen because it can carry all three satellite payloads in one launch, thus eliminating the need for multiple launches.

Starting from 2008, Soyuz launch vehicles can now be commercially launched from the Guiana Space Center, Kourou. Arianespace launch vehicles were chosen as they are efficient boosters for low-inclination missions. Their Kourou launch site is just 5° north of the equator. This will be a huge cost-saver during the design process for our propulsion subsystem, as only minimal orbit insertion maneuvering is required. We note here that an inclination change of one degree requires about 208 m/s of velocity in LEO. We can get the best performance from a launch vehicle into a direct, low-inclination LEO orbit that we desire from the Kourou launch site. This takes advantage of the easterly velocity from Earth's rotation, saving costs of launching and orbit maneuvering. This is further backed by Arianespace's success in the commercial space flight industry, largely due to the strategic launch location and long history of launch successes. The Soyuz launch vehicle complements the Ariane5 and Vega class launch vehicles offer in the medium-weight payload class for LEO orbit, which suits our requirements for orbit insertion for an approximately 600 km LEO orbit.

Furthermore, the long history of the Soyuz-class launch vehicles' exceptional performance (over 1200 successfully launches) is also a large pull factor when considering the probability of mission success and expertise on adapting different spacecraft payloads to the launch vehicle. Moreover, the cost of launching is significantly lower than most other launch vehicles.

4.7.b Weather considerations

Bad weather can severely restrict changes to launch, thus costing time and money. For the French Guiana in our case, many thunderstorms and frequent lightning during the spring and summer are our main concerns because the highly ionized gas in the launcher's exhaust plume can attract lightning. Thus, we must launch carefully in these seasons if our client decides to do so. During the winter, the winds aloft are severe because the jet stream moves to the south and often pass over both the Eastern and Western Ranges. In order to maximize safety, we should study weather information to select the best launch date, balancing out cost and timeline considerations.

4.7.c Payload adaptor

For the trailing microsattellites with the main function of SAR Interferometry, they will be attached to the ASAP adaptor while the main satellite will be fitted with the options provided by Arianespace. It is understood that the adaptors will include either pneumatic or spring-based actuators to separate the payload from the launch vehicle. For redundancy, we will add an additional spring-based deployment mechanism for separation in case the primary pneumatic actuator provided fails (in any case, we will still deploy the secondary spring-based component as it is not useful). The ADCS will then take over and separate from the payload adaptor and launch vehicle components.

Chapter 5

System overview

5.1 Contingency

Application of contingencies and margins ensures that uncertainties in early stage design work can be accounted for. Consequently, growth in the system later in the design process will not have as adverse an effect as it might otherwise. Contingencies in this design are applied to mass, power, telecommunications and other systems. We used a contingency of 35% for our satellite mass.

5.2 System overview

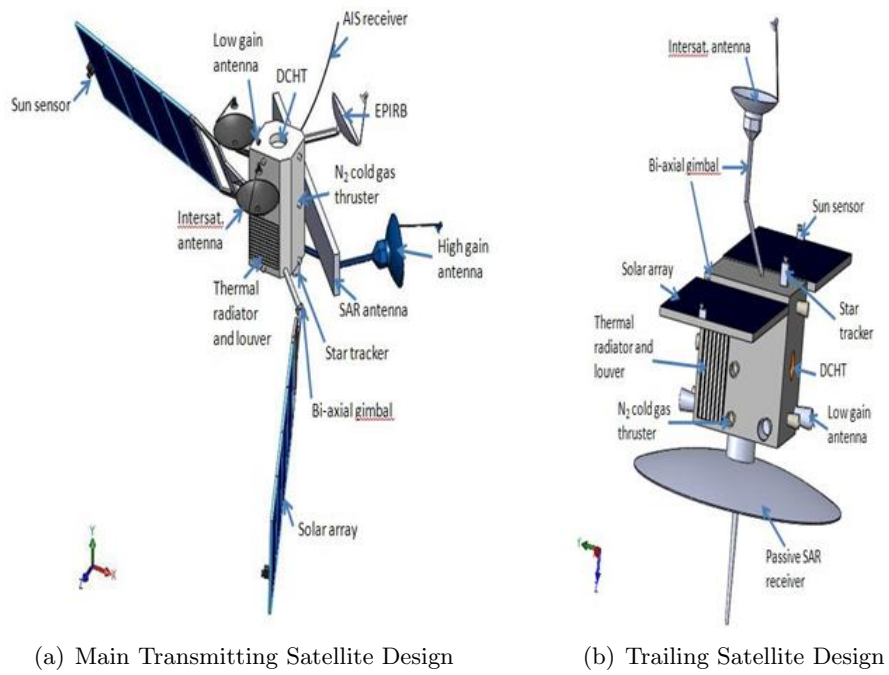
Please refer to Tables 11 and 12 and Figure 13.

Subsystem (Main Satellite)	Quantity	Mass (kg)	Subsystem (Microsatellite)	Quantity	Mass (kg)
ADACS		50	ADACS		30
i) Star Sensors	1		i) Star Sensors	1	
ii) Sun Sensor	1		ii) Sun Sensor	1	
iii) Tri-axis Rate Gyros	2		iii) Tri-axis Rate Gyros	2	
iv) N ₂ thrusters	12		iv) N ₂ thrusters	12	
v) Gimbals					
C&H	1	4	C&DH	1	1.5
i) On-board computer			i) On-board computer		
Payload		400.25	Payload		12
i) Phased Array active SAR transmitter (dual polar)	1		i) Phased Array active SAR receiver (dual polar)	1	
ii) EPIRB parabolic antenna	1				
ii) AIS horn antenna	1				
Power		50	Power		8.5
Structures		50	Structures		7
Propulsion		50	Propulsion		5
Telecom		10.8	Telecom		2
i) High gain X-band parabolic antenna	1				
ii) Low gain X-band horn antenna	4		ii) Low gain X-band horn antenna	4	
iii) Low gain K-band parabolic antenna	2		iii) Low gain K-band parabolic antenna	2	
Thermal		15.6	Thermal		12.8
Adadpter (launch vehicle)		5.3			
Contingency		222.3	Contingency		27.580
Total injected mass		857.7	Total injected mass		106.38

Table 11: System mass overview

	Bus (m)	Solar-Array (each)
Main satellite	$1.20 \times 1.20 \times 2.00$	1.94×3.86
Microsatellite	$0.600 \times 0.600 \times 1.200$	0.89×2.54

Table 12: Satellite Dimensions



(a) Main Transmitting Satellite Design

(b) Trailing Satellite Design

Figure 13: Satellite design models of the transmitting satellite and microsatellite

Chapter 6

Propulsion

6.1 Introduction

As Arianespace Soyuz launch vehicle provides accurate launch to the desired circular LEO orbits for our initial mission, we need only consider the orbit maintenance and de-orbit of the mission phase for the usage of the propulsion subsystem for the main transmitting satellite. For the microsatellite formation, we need to add the ΔV of the orbital maneuvering for the flying formation into the calculations.

To maintain our complex fly formation, a strong, reliable and lightweight propulsion system must be used. For the conceptual design of the propulsion subsystem, several different architectures were examined. We consulted the MIT Space Propulsion Laboratory for expertise on the propulsion subsystem architectures due to their experience on developing the Diverging Cusp Hall-effect Thruster (DCHT). Different architectures (chemical and electric) were compared based on the figures of merit mass, cost, volume, risk and flight time.

6.2 Architecture trade studies

In our project, we have conducted extensive studies on the propulsion system. We have chosen the Hall-effect thrusters over chemical propulsion systems due to concerns over safety, and due to mass and cost considerations (see Appendix K). The electronic propulsion subsystem will run off the solar arrays in sunlit portions of the trajectory and the batteries in the shadow portion. The use of payload battery power for electric propulsion is described in the power subsystem section .

6.3 Hall effect thruster

The thruster chosen will be a diverging cusped-field Hall-effect thruster (DCHT) based on the work of Dan Courtney of the MIT SPL (see Figure 14). This thruster is chosen based on efficiency, reliability and cost-effectiveness. For more information on the mechanism of the Hall thruster effect, please refer to Appendix L.

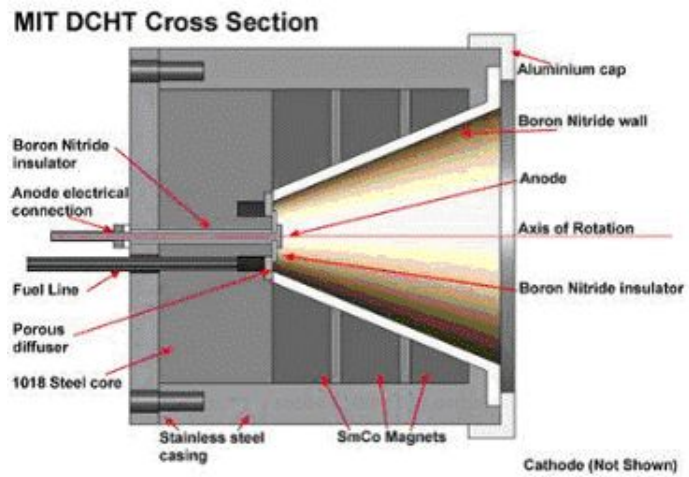


Figure 14: DCHT thruster [courtesy of Dan Courtney]

Chapter 7

ADCS and orbit control

SAR mission requires a great level of precision in attitude and orbital controls. Thus, a great emphasis has been placed on the ADCS and OCS so that our satellites can successfully execute the mission. A number of sensors and equipments have been chosen to provide the needed accuracy and precision.

7.1 Overview of spacecraft configuration options for the main satellite

Configuration features:

Equipment Compartment Rectangular.

Solar array Deployed planar panels on diagonal sides of body, dual-axis articulation (Honeybee Robotics).

Appendages One steerable high-gain communications instrument package.

Attitude control 2-axis for solar array, 3-axis control using reaction wheels and cold gas thrusters, 1-axis in direction of flight.

7.2 ADCS requirement for the main satellite

The requirements are listed in Table 14.

7.3 Selection of spacecraft control type for the main satellite

Detailed descriptions on each component are presented in Appendix M. Detailed methods for the deployment mechanism are found in Appendix U.

Item	Requirement
Pointing	Pointing accuracy of $\pm 1^\circ$ in the x and y direction for all engines. Pointing accuracy of $\pm 20^\circ$ in the z direction for solar panels
Launch vehicle separation	Depending on ΔV .
Sensing	Depending on sensors equipment. Run a control cycle once every cycle period. Provide an attitude measurement from the external sensing equipment (star tracker and sun sensors) every minute.
Disturbance control	Limit drift to $5^\circ/\text{h}$ to a max of $\pm 1^\circ$ in the x or y direction and 20° in the z direction. Torques from cyclic external disturbances: solar radiation and magnetic field. Torques from constant external disturbances: gravity gradient and aerodynamic drag. Torques from the following internal disturbances: uncertainty in the center of gravity, thruster. Misalignment, thruster minimum impulse bit deadbanding.
Duration	Provide active attitude control and sensing for a duration of at least 5 years. Must provide a combination of passive and active attitude control and sensing for a duration of at least 5 years in LEO for its imaging/communication relay purposes.

Table 13: ADCS requirements for the main satellite

Item	Parameters
Attitude sensors	<ul style="list-style-type: none"> • Star sensor Providing high precision and accuracy. Coupling with gyroscopes for rapid response. • Sun sensor Consisting of four photodiodes (two in the x-axis, two in the y-axis). 2 W at 40 g.
Rate gyros	Consisting of two tri-axis solid state rate gyros.
Reaction wheel	Four of these reaction wheels, one for each direction and one for redundancy.
Actuators	Consisting of twelve N_2 thrusters.
Engine Gimbal	Included to stabilize the satellite.
Antenna Gimbal	Included to stabilize the satellite.

Table 14: Spacecraft control type for the main satellite

7.4 Overview of spacecraft configuration options for trailing microsatellites

Configuration features

Equipment Compartment Rectangular.

Solar array Deployed planar panels on diagonal sides of body, dual-axis articulation (Honeybee Robotics).

Appendages Two SAR antennas.

Attitude control One face toward nadir, 2-axis for solar array, 3-axis control using cold gas thrusters, 1-axis in direction of flight.

7.5 Selection of spacecraft control type for trailing satellite

The control types of the trailing satellites are the same as the main satellite. This includes a star sensor, sun sensors, rate gyros, reaction wheels, actuators, antenna gimbals and engine gimbals.

7.6 Orbit Determination and Control

The primary method for orbit determination is through the use of onboard Global Positioning System (GPS) receivers, and by Precision Orbit Determination software which will be implemented by MDA. Orbit control is achieved by the propulsion system. Orbit determination GPS systems will be installed in both the main satellite and microsatellites.

Fast-delivery position knowledge	± 60 meters (3σ in each axis)
Post-processed position knowledge	± 15 meters (3σ in each axis)

Chapter 8

Communication subsystem

To maintain the formation, the satellites also need to communicate effectively with each other and with the ground stations. The communication must be completely secured so that an immediate response can be executed.

8.1 Objective

- Satellite must be able to pick up distressed signals and calculate the coordinate of distressed vessels in less than 10 minutes.
- Satellite must be able to establish low gain communication with the ground station in any orientation.
- Satellite must be able to establish high gain communication with the ground station in nadir orientation.
- Satellite must be able to provide near real-time imaging to the ground station to conduct search and rescue operation.

8.2 Frequency selection: X-band and Ku-band are popular as LEO frequency

The two options for the HGA frequency are either X-band (8.4 GHz uplink & 7.45 GHz downlink) or Ku-band (14.4 GHz uplink & 11.7 GHz downlink). However, the Ku-band is not desirable due to the high amount of atmospheric and rain attenuation of around 20 dB to 30 dB experienced in the region of the Straits. On the other hand, the X-band atmospheric and rain attenuation is around 5 dB to 10 dB. Hence, X-band communications will provide a high margin and reliability at a lighter satellite and lower cost compared to the Ku-band.

The main station will be at the Singapore Global Maritime Distress & Safety System (GMDSS) monitoring station. Other X-band ground stations in the regions include the Malaysian Center for Remote Sensing, Temerloh, Pahang; the Singapore Centre for Remote Imaging, Sensing and Processing; and Indonesia National Institute of Aeronautics and Space, Biak.

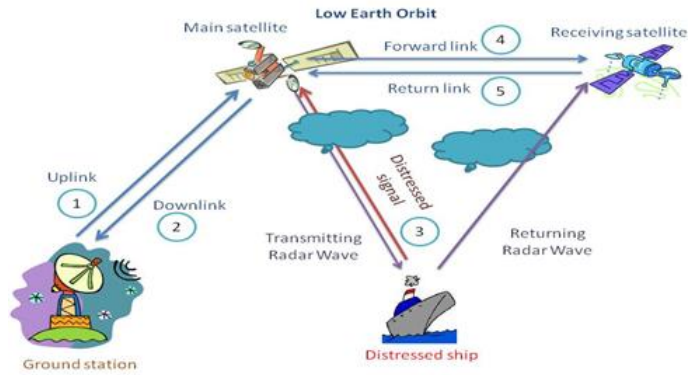


Figure 15: Communication concept operation. For simplicity the communication only features two satellites in action. The images are for demonstration purposes and therefore not scaled models of our satellites.

8.3 Concept operation

Please refer to Table 15.

8.4 Communication payload

8.4.a Link budget calculation

According to the frequency, antenna gains and antenna are calculated in Appendix V.

8.4.b Main satellite

Downlink high-gain antenna configuration The parabolic reflector with offset feed is chosen as the high gain antenna because it can provide high gain with a focused beam, low aperture blockage and reduced sidelobe levels. Complete calculations are presented in Appendix S.

Downlink low-gain antenna configuration The horn antenna is chosen to provide low gain connection with wider beamwidth because it is relatively simple and low weight.

Intersatellite link K-bands (60 GHz or 125 GHz) are usually chosen as intersatellite link. In our system, the satellite formation is quite tight; the average distance between the main satellite and the receiving satellite is about 10 km. The satellite movement needs frequent correction and 60 GHz is chosen as it provides high gain at wider beamwidth. An alternative method of using optical/laser instruments is documentd in Appendix T.

The antennas are described in Table 16.

8.4.c Trailing satellites

The antennas on the trailing satellites are described in Table 17.

Link	Type	Frequency	Description
1	Uplink	8.0 GHz	Communication from the ground station to the main satellite. Delivers commands, provide tracking and telemetry of the main satellites.
2	Downlink	7.5 GHz	Communication from the main satellite to the ground station. Delivers sensor data, images, ship location.
3	Distressed signal	406 MHz	Distressed signal [EPIRB or AIS] from a vessel. The distressed signal will be picked up by the main satellite receiver in less than 10 minutes.
4	Forward link	60 GHz	Communication from the main satellite to the receiving satellite. This communication provides command and telemetry, keeping the satellites in close formation.
5	Return link	60 GHz	Communication from the receiving satellite to the main satellite. This communication transfers collected data over the high.

Table 15: Link descriptions

Link	Type	Frequency (Ghz)	Gain (dBi)	Beamwidth (°)	Mass (kg)	Size (m)	Quantity
Downlink	Parabolic [steerable]	7.5	36 to 38	1.6	5.8	1.0 dia	1
Downlink	Horn	7.5	17 to 18	22 to 23	0.25	0.12 × 0.12	5
ISL	Parabolic reflector	60	47.34	0.7	2	0.5 dia	2

Table 16: Calculated antenna configuration for the main satellite [from Larson and Wertz [36]]

Link	Type	Frequency [GHz]	Gain [dBi]	Beamwidth [°]	Mass [kg]	Size [m]	Quantity
Downlink	Horn	8	17 to 17	22.38	0.25	0.12 × 0.12	5
ISL	Parabolic reflector	60	47.34	0.7	2	0.5	1

Table 17: Calculated antenna configuration for the trailing satellite [from Larson and Wertz [36]]

8.4.d Transmitter configuration for main satellite

Item	Quantity	Mass [each]	Power [each]
Intersatellite link	2	6 kg	100 W to 120 W
Downlink	1	< 1 kg	30 W to 40 W

8.4.e Transmitter configuration for the trailing satellite

Item	Quantity	Mass [each]	Power [each]
Intersatellite link	1	6 kg	100 W to 120 W

Chapter 9

Command and data handling system

System complexity has large influence on the design of CDHS. See Tables 18 and 19.

Requirement/constraint	System complexity	
	Receiving satellites	Main satellites
Processing commands		
CMD rates	50 cmd/s	≥ 50 cmd/s
Computer interface	Computer or stored	Yes
Stored commands	cmds (not both)	Not needed
Number of channels	300 channels to 500 channels	≥ 500 channels
Processing of telemetry data		
TLM rates		
Housekeeping data	4 kbps to 64 kbps	64 kbps to 256 kbps
Payload data	1 kbps to 200 kbps	10 kbps to 10 Mbps
Computer interface	None	Yes
Number of channels	400 channels to 700 channels	> 500 channels
Other		
Mission time clock	Included	Included
Computer watchdog	Included	Included
ACS function	None	Included
Bus constraints	Single unit	Integrated unit
Reliability-class B parts		
Single string	0.7610	0.6983
Redundant	0.9736	0.9496
Reliability-class S parts		
Single string	0.9083	0.8286
Redundant	0.9964	0.9496
Radiation environment (total dose)	2 krads to 50 krads	50 krads to 1 Mrads
Schedule (in months, after order)		
Class B parts	6 to 12	9 to 18
Class S parts	9 to 24	9 to 24

Table 18: Command and Data Handling subsystem estimation [Larson and Wertz [36]]

		Microsatellite	Main satellite
Size (cm ³)	Command only	2000 to 4000	5000 to 6000
	Telemetry only	4000 to 6000	9000 to 10 000
	Combined system	6000 to 9000	13 000 to 15 000
Weight (kg)	Command only	1.5 to 3.0	4.0 to 5.0
	Telemetry only	2.5 to 4.0	6.5 to 7.5
	Combined system	4.5 to 6.5	9.5 to 10.5
Power (W)	Command only	2	2
	Telemetry only	10 to 16	13 to 20
	Combined system	13 to 18	15 to 25

Table 19: Parametric estimation of C&DH size, weight and power [Larson and Wertz [36]]

Chapter 10

Power subsystem

The power system is the backbone of the mission. Without a reliable power source the satellites will fail to operate. Choices of other subsystems have great influence on power. We have extensively analyzed the requirements of each subsystem at different phases and evaluate suitable power solutions.

10.1 Power requirements

The requirements are shown in Table 20.

As discussed previously, the mission duration is split into 8 phases for better management of satellite subsystem operations. Power during phase 1 will be provided by the launch vehicle. Power during phases 2 and 7 will be provided by primary batteries. Power during phases 3 and 4 will be provided by the solar arrays. Part of this energy will be used to recharge the battery, which will power the satellite during phases 4 and 6.

10.1.a Solar arrays

The requirements are described in Table 21.

State-of-the-art Emcore's BTJ triple junction InGaP/InGaAs/Ge solar cells with n-on-p polarity on 140 μm uniform thickness substrate were chosen due to superior efficiency (28.5% at 280 $^{\circ}\text{C}$), excellent radiation resistance ($P/P_0 = 0.89$ at 1 MeV equivalent fluence of $5 \times 10^{14} \text{ e/cm}^2$), low temperature coefficient ($-0.064 \text{ abs } \%/^{\circ}\text{C}$), light weight (84 mg/cm²) and high mechanical strength.

The solar arrays wrap around the vehicle during launch, with one panel forming each side of a box. They are secured in place using Dyneema wire under pretension. To break the wire, two small redundant resistors on each wire will melt through the wire at 150 $^{\circ}\text{C}$. When released from vehicle, torsion springs will unfold the panels, and damping mechanisms will critically damp the panels' motion such that they can get into place when they reach $\pm 180^{\circ}$. There will be no locks in case they damage the solar panels. Two micro-switches will also be embedded in the hinge to detect stowed and deployed positions for redundancy and safety.

10.1.b Primary batteries

The requirements for primary batteries are shown in Table 22.

During phases 2 and 7, the primary battery is the power source. The solar array might not have been deployed during phase 2 and discharging the secondary battery may not be suitable due to its

Peak power	phase 1	phase 2	phase 3	phase 4	phase 5	phase 6	phase 7	phase 8
ADCS	NA	81	81	81	81	81	81	NA
C&DH	NA	25	25	25	25	25	25	NA
SAR	NA	0	4000	0	4000	0	0	NA
AIS	NA	0	0.18	0	0.18	0	0	NA
Distress receiver	NA	0	1	0	1	0	0	NA
Communication	NA	820	1160	0	1160	0	1160	NA
Propulsion	NA	250	100	0	100	0	250	NA
Power	NA	5	10	10	5	5	5	NA
Thermal	NA	5	5	5	10	10	5	NA
Structure	NA	0	0	0	0	0	0	NA
Total	NA	1186	5382.18	121	5382.18	121	1526	NA

Table 20: Peak power requirements for the main satellite (in W)

Solar array	Main satellite	Microsatellite
Area (m ²)	4.42	1.72
Mass (kg)	3.71	1.44
Power output BOL (W)	1722	670
Power output EOL (W)	1300	500
Cost (S\$)	2.48 million	0.97 million

Table 21: Solar array requirements for main satellite and trailing satellite

Primary battery	Main satellite	Microsatellite
Capacity (Wh)	1000	830
Mass (kg)	3	2.4
Cost (S\$)	200 000	160 000

Table 22: Primary battery requirements for the main satellite and the trailing satellite

Secondary battery	Main satellite	Microsatellite
Capacity (Wh)	2150	560
Mass (kg)	12.3	3.2
Cost (S\$)	220 000	60 000

Table 23: Secondary battery requirements for the main satellite and the trailing satellite

Battery charger	Main satellite	Microsatellite
Capacity (Wh)	33	9
Mass (kg)	11	3.5
Cost (S\$)	8600	2500

Table 24: Battery charger requirements for the mains satellite and the trailing satellite

low specific energy. In phase 7, the solar array may not deliver enough power effectively and reliably in due to unavoidable lifetime degradation. Lithium-ion primary battery produced by ABSL Space Product will be chosen due to high specific energy density, light weight and proven flight record and reliability in energy-intensive missions.

10.1.c Secondary batteries

The requirements for the secondary batteries are shown in Table 23.

VES180 rechargeable lithium ion cells produced by Saft were chosen due to their long lifetime (60 000 cycles in LEO at 20% DOD), high energy density (180 Wh/l), high specific energy (175 Wh/kg) and nearly 100% charging efficiency. The battery will be made up of battery packs, each containing 3.6 V cells placed in series to form a 28 V pack.

10.2 Power distribution system

10.2.a Architecture

Both the main satellite and microsatellites employ a 28 Vdc unregulated bus with Direct Energy Transfer (DET) energy regulation scheme for its higher efficiency because they dissipate little energy by simply shunting excess power at the array through shunt resistor banks. Linear and switching shunt systems are combined in a multistage sequential topology.

10.2.b Battery chargers

The requirements are shown in Table 24.

The batteries are charged independently by linear, charge-current control (LC^3) to ensure batteries lifetime greater than five years because when batteries are charged in parallel, the voltage is the same but the current and temperature are not. Parallel batteries eventually end up balancing out and so have a lifetime of under five years. Independent charging also optimizes battery usage by charging each battery to its own limit and forgives battery deviations in systems with many batteries. In addition, every cell will have a bypass diode in the event of cell-failure.

10.2.c Converters

The power system will service the subsystem at four discrete voltages. The propulsion system itself will step up/down voltages within the propulsion system itself. Converters are purchased from Vicor.

DC/DC converters	Main satellite	microsatellite
Capacity (Wh)	15	13
Mass (kg)	3	3
Cost (\$)	2500	2400

We show extensive studies on our choice of instruments in Appendix Q.

Chapter 11

Thermal subsystem

The thermal subsystem provides critical cooling for the satellites. Its requirements are derived from previous chapters.

11.1 Radiators

Body-mounted radiators are used to reject waste heat to space. The radiator is made up of aluminium honeycomb coated with Optical Solar Reflector (OSR) 8 mil quartz mirror with BOL (beginning of life) $\alpha = 0.8$, EOL (end of life) $\alpha = 0.11$ and $\varepsilon = 0.80$.

Radiators	Main satellite	Trailing satellite
Area (m ²)	1.5	1
Mass (kg)	5	3.3
Cost (S\$)	6000	5000

11.2 Louvers

Radiators will be fitted with louvers purchased from Orbital Sciences Corp. to control the rate of heat dissipation when the temperature drops during eclipses.

Louvers	Main satellite	Trailing satellite
Mass (kg)	4.8	4.5
Cost (S\$)	3000	2700

11.3 Insulation

The entire surface area of the satellite, except for radiators, are covered with 15-layer Kapton Multilayer Insulation (MLI).

Multilayer insulation	Main satellite	Trailing satellite
Area (m ²)	8	5
Mass (kg)	5.8	3.6

Chapter 12

Cost analysis

Cost estimation is crucial to the project because we need to stay within the limited budget. To give an accurate assessment, we use the parametric cost estimation relationship from a public model like the Unmanned Space Vehicle Cost Model and Small Satellite Cost Model from Larson and Wertz [36]. Final figures are adjusted for inflation and currency conversion. For details, refer to Tables 25 and 26.

- Launching cost: S\$51 726 500.
- Software cost: S\$2 500 000.
- Ground station construction: S\$20 000 000.
- Maintenance over a period of 5 years: S\$65 000 000

Total cost of design and maintenance = S\$286 564 741 = S\$286.6 million

Subsystem	Cost component	Data	RDT&E	TUC1	TUC2	Total cost
Payload	SAR transmitter	30 000 000	18 000 000	30 000 000	27 000 000	75 000 000
	Structure	392	22 301	5135	4622	32 058
Spacecraft bus	Thermal	48	4603	781	703	6088
	EPS	34	2121	1645	1480	5247
	TTC&DH	13	3725	2666	2399	8790
	ADCS	53	14 584	6439	5795	26 817
IAT		47 335	11 166	492 285	443 056	946 507
Program level		47 335	16 778	16 141	14 527	47 447
Ground support equipment		47 335	9293	0	0	9293
Launch and orbital ops support		1000	0	4900	4410	9310
Total						76 091 557
Adjusted for inflation [S\$]						134 834 399

Table 25: CER for the main satellite. Abbreviations: RDT&E (Research, Development, Testing and Engineering), TUC (Theoretical Unit Cost).

Subsystem	Cost component	Data	RDT&E	TUC1	TUC2	Total cost
Payload	SAR receiver	400 000	240 000	400 000	360 000	1 000 000
	Structure	392	22 301	5135	4622	32 058
Spacecraft bus	Thermal	48	4603	781	703	6088
	EPS	10	648	666	599	1913
	TTC&DH	7	2396	1918	1726	6040
	ADCS	53	14 584	6439	5795	26 817
IAT		284 533	62 164	2 959 143	2 663 229	5 684 536
Program level		284 533	75 831	97 026	87 323	260 180
Ground support equipment		284 533	29 394	2450	2205	34 049
Launch and orbital ops support		1000	0	2450	2205	4655
Total						7 056 336
Adjusted for inflation [S\$]						12 503 842

Table 26: CER for the trailing satellite. Abbreviations: RDT&E (Research, Development, Testing and Engineering), TUC (Theoretical Unit Cost).

Chapter 13

Conclusion

Our solution to the competition challenge is a novel and robust satellite system consisting of one main transmitter satellite and two passive receiver trailing satellites in flying formation launched into 600 km equatorial orbit via the Soyuz launch vehicle. The satellite system has an effective coverage time of 99.54 mins (5972 sec), 28 revisits per day, and a payload resolution of 1.1 m (max. azimuth resolution) with 24 hour coverage. The total injected mass of the transmitter satellite is 857.70 kg and of the trailing satellite is 106.38 kg each. The payload onboard the transmitting satellite consists of a Dual Polarized Phased Array Synthetic Aperture Radar Transmitter, an AIS receiver and a 406 MHz distress signal receiver. The payload onboard the trailing satellites are Dual Polarized Synthetic Aperture Radar Receivers. The distress signal activation time was 15.2 minutes, well within competition specifications. The total cost of designing and maintaining the satellite formation is S\$286.6 million, within the proposed budget.

Appendix A

AIS Ship tracking

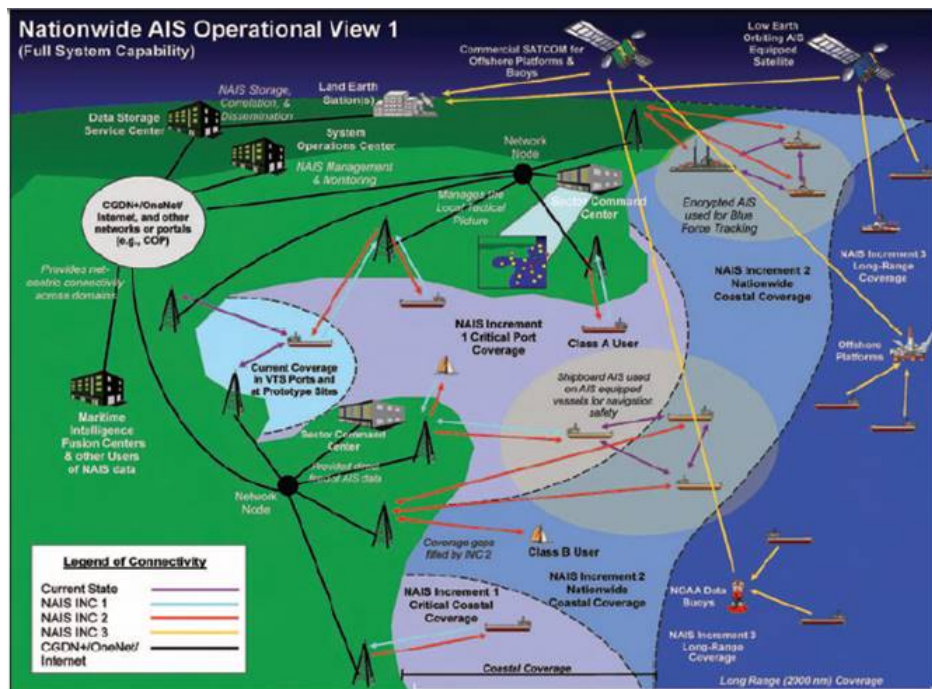


Figure 16: A USCG outline of how the satellite network will be expected to collect and forward AIS data.



Figure 17: AIS Ship tracking software at user terminal



Figure 18: AIS user transponder on ship

Appendix B

Cospas-Sarsat emergency beacons

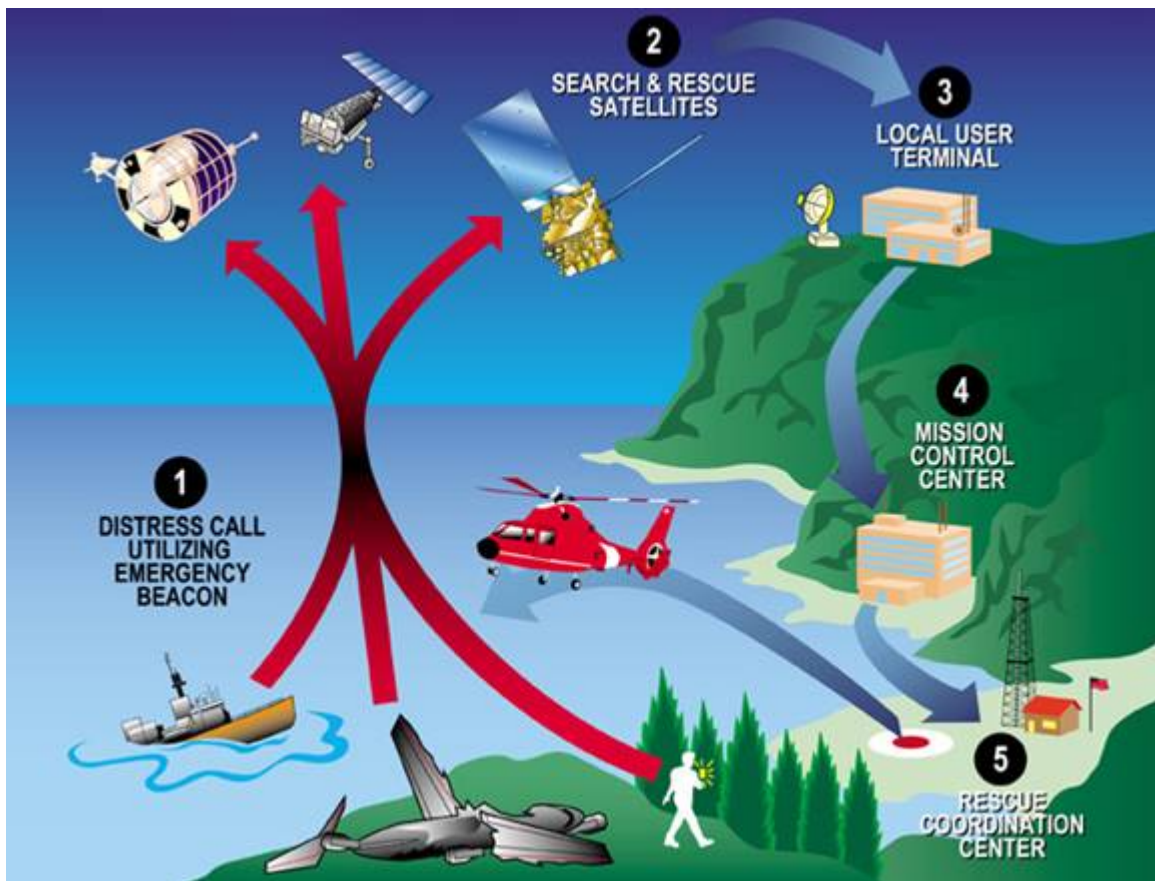


Figure 19: Emergency beacons signal relay from distress site, through satellite to user terminal

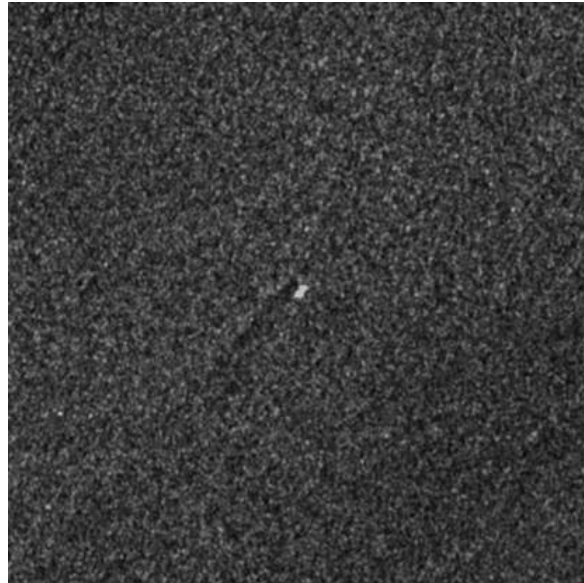


Figure 20: EPIRB emergency transponder

Appendix C

A single SAR system

Synthetic aperture radar (SAR) is a coherent side-looking radar which builds a large aperture along its flight path by means of a computer measuring and storing amplitude, frequency, phase, and polarization of signals reflected from observed targets or pixels on the ground respectively. The length of the synthetic aperture is determined from the dwell time on a single pixel depending on the width of the real antenna beam for the range gate which houses the pixel. The system utilizes the Doppler frequency for pixel positioning. That is, it uses the effect whereby targets perpendicular to the satellite flight path at some instant in time have return signal frequencies equal to the Doppler center frequency (DCF) and targets fore (aft) of perpendicular have greater (lesser) frequencies, respectively. $DCF = 0$ for a strictly side looking SAR. During processing all signals with $DCF=0$ will be arranged on a line perpendicular to the flight pass. SAR images three dimensional targets, especially land and sea surfaces, in two dimensional maps. Each pixel within the map is complex consisting of amplitude and phase. Therefore, both the amplitudes and the phases can be arranged to a two dimensional image of the observed scene.



Appendix D

Problems with a single SAR system

SAR images show some typical specialties compared to optical images. The azimuth resolution of SAR is independent from range which leads to a lack of perspective. Therefore, SAR images of three dimensional landscapes look like two dimensional maps. However, there is no resolution in elevation. The special SAR geometry causes special image errors like shadowing, fore shortening and lay over (see Figure 21). Radar shadows are areas with no radar signal return. Here the signal-to-noise ratio is zero ($SNR=0$). Foreshortening and layover are look-angle effects which cause relief displacements of three-dimensional objects like mountains, towers and so on. Foreshortening causes a compression of the areas with ascending slope and a spread of the descending slope. When lay over effects occur, several areas can disappear from the SAR image.

A simple but effective SAR processing model considers it as a Microwave Transducer (MT) which observes the real world's reflectivity in order to produce an estimate of it. This output is called SAR image I and represents an estimate of reflectivity. An SAR Imaging System is based on two different data acquisitions for along-track (azimuth) and slant range scanning. Such an MT is not perfect. In particular, its ability to spatially resolve two points on the image is not arbitrarily fine. Resolution is the quantity used to measure such a limitation. The generated image (i.e. the backscattering reflectivity estimate) is affected by a multiplicative noise—the so-called speckle which arises from the interference of the elementary returns within each resolution cell (Raney [48])—because SAR is a coherent system.

During rough seas, the contrast between the ships and the sea will be significantly compromised because the sea surface also becomes rough, leading to numerous false detections of ships.

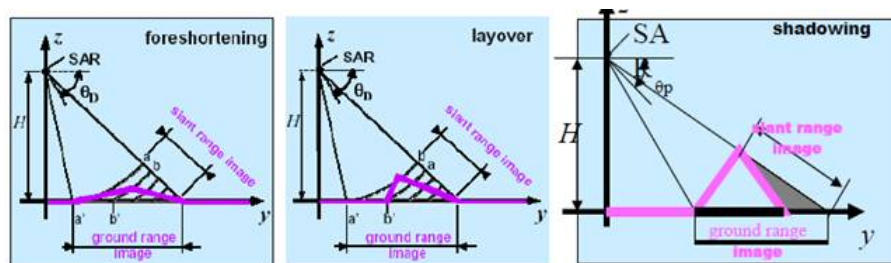


Figure 21: Geometric distortions in SAR Images. Foreshortening: slope of local terrain is less than incidence angle leading to layover for steep terrain (slope of local terrain is less than incidence angle). Shadowing: descending slope is less than incidence angle, $SNR = 0$, no signal.

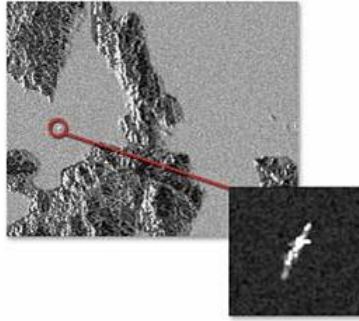


Figure 22: A typical RadarSat 1 SAR imagery of a ship in relatively rough water conditions.

In Figure 22, it is hard to differentiate the bright spot (target ship) from the clutter. Since one of our primary aims to track pirate ships, a simple SAR system is not enough to monitor such small targets which very small ship makes. Most of the time, they will not register in the SAR image.

Appendix E

Polarimetry

Polarization is the orientation of the electric field vector (\mathbf{E}) in an electromagnetic wave, frequently denoted “horizontal” (H) or “vertical” (V) in conventional imaging radar systems. Polarization is established by the antenna, which may be adjusted to be different on transmit and on receive. Reflectivity of microwaves from an object depends on the relationship between the polarization state and the geometric structure of the object. Common shorthand notation for band and polarization properties of an image file is to state the band, with a subscript for the receive and the transmit state of polarization, in that order. Thus, for example, LHV indicates L-band, horizontal transmit polarization, and vertical receive polarization. Possible states of polarization in addition to vertical and horizontal include all angular orientations of the \mathbf{E} vector, and time varying orientations leading to elliptical and circular polarizations. (Henderson and Lewis [29]) Principally holds: Each scatterer is a polarization transformer. Polarimetry is the measurement of the polarization properties of an electromagnetic wave.

The complete state of a scattered Electromagnetic Wave can be described by the Scattering Matrix \mathbf{S} which connects the received field vector \mathbf{E}_r with the transmitted field vector \mathbf{E} (Boerner [4])

$$\begin{bmatrix} E_H^r \\ E_V^r \end{bmatrix} = [S] \begin{bmatrix} E_H^t \\ E_V^t \end{bmatrix} = \begin{bmatrix} S_{HH} & S_{HV} \\ S_{VH} & S_{VV} \end{bmatrix} \begin{bmatrix} E_H^t \\ E_V^t \end{bmatrix} \quad (\text{E.1})$$

The complex scalar components of the electric field vector can be expressed as

$$E_p^k = |E_p^k| e^{i\varphi} \quad (\text{E.2})$$

p characterizes the polarization and $k = t, r$ the different “directions” (transmit t , receive r). The elements of the matrix \mathbf{S} are complex also and, therefore, the matrix contains 8 independent parameters. These figure reduces to 5 independent parameters in case of backscattering and if the reciprocity theorem holds i.e. for $S_{VH} = S_{HV}$.

The phase decomposition which can be performed in polarimetric SAR can estimate for three orthogonal scattering mechanisms (Cloude and Pottier [9]). For example, in a simplified model the three different scattering mechanisms can be described as: 1) a single bounce contribution from point scatterers, 2) a double bounce contribution from vertical structures like house walls and so on, and 3) a diffuse (volume) contribution from statistical distributed scatterers like tree leaves and branches. The respective Pauli matrices are:

$$\mathbf{S}_1 = \begin{bmatrix} 1 & 0 \\ 0 & 1 \end{bmatrix} \quad \mathbf{S}_2 = \begin{bmatrix} \cos 2\alpha & \sin 2\alpha \\ \sin 2\alpha & \cos 2\alpha \end{bmatrix} \quad \mathbf{S}_3 = \mathbf{S}_{\text{diffus}} = \begin{bmatrix} 0 & 1 \\ 1 & 0 \end{bmatrix} \quad (\text{E.3})$$

This formulation of the 3 matrices takes into account the influence of the lateral horizontal incidence angle α at extended long line scatterers, structures like fences, long walls and so on. However, it is not possible with this technique to separate the contributions of the same scattering mechanism distributed over different heights. These topics are presented in Boerner [4] and Pottier et al. [46].

Appendix F

SAR interferometry

Our main concern about a single SAR based system is sorting out ships from the noise in a large swath area. Generally speaking, ship detection is limited by noise, clutter, in-homogeneities, features and artifacts in the image background, which hamper detection of the weakest targets or cause false alarms.

Commonly, a single SAR satellite system combats this problem by using SAR Interferometry by analyzing the phase difference of two received radar echoes of a single target at different satellite positions to create Digital Elevation Maps (DEM) interferograms (see Figure 23) that are known to detect height differences in the terrain within an accuracy of a few meters. But this precision in height accuracy is only limited to stationary terrain. In this scenario, the satellite uses a ‘repeat-pass’ mode to create the DEM, notes the phase of the received radar echo from the specified target and revolves around the earth until it can get the phase of the second radar echo. The phase difference is then analyzed.

To overcome this limitation of inaccurate DEMs formed by repeat-pass inSAR, receiving interferometric data in a single pass by using two or more independent radar satellites operating in a fully or semi-active SAR mode (Das and Cobb [12], Martin et al. [39], Massonnet [42], Zebker et al. [53]) is needed. The concept is still the same as a repeat-pass SAR system. However, instead of orbiting around the earth to get the phase of the second radar echo, two additional satellites are used (see Figure 24), positioned at predetermined locations around the main transmitting SAR satellite

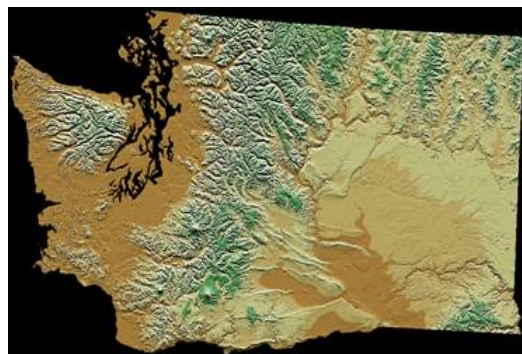


Figure 23: An example of a DEM taken by a SAR satellite in repeat-pass mode (note: falsely colored).

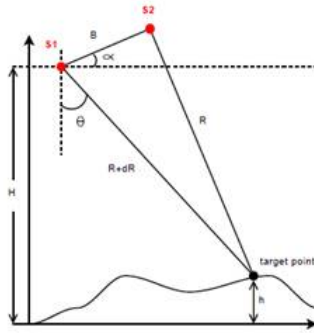


Figure 24: A basic 2-D SAR interferometry geometry showing two satellites S1 and S2 receiving a reflected signal from a target point on the ground.

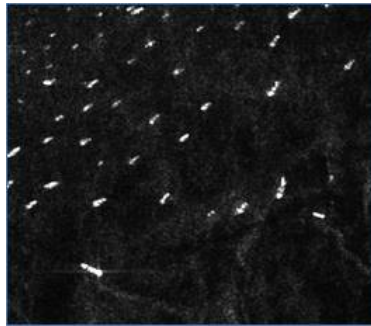


Figure 25: DEM of ship vessels in coastal waters. Compared to the background, the targets are prominently detected.

that will immediately calculate the phase difference of a target (since the two receiver satellites are in different locations), removing the hassle of taking a second reading as in the conventional way.

The idea of using these passive micro-satellites flying in formation with a conventional SAR, as introduced by Massonnet [42], is especially attractive because it will enable a cost-efficient implementation of a highly capable interferometric single-pass SAR system in space. Different receiver configurations can be used to produce digital elevation models, accurately detect moving objects on the ground, produce super resolution imagery, or measure temporally changing terrain features. Moreover, interferometric data from single-pass SAR systems are very accurate at detecting moving objects (see Figure 25) and their applications also include oil spill detection.

The reason for main emphasis on single-pass interferometric DEMs is that they can very easily detect slight irregularities in the terrain, perfect for maritime surveillance where the generally open, flat terrain of the sea/ocean is compared with the sudden increase in height difference of a moving vessel that is floating. Moreover, the height accuracy is so good that the difference in height level of oil on water can be detected to monitor oil spills in the region for environmental purposes.

Two relationships are obtained from the above diagram:

$$\sin(\theta - \alpha) = \frac{\left[R - \frac{\lambda\phi}{4\pi}\right]^2 - R^2 - B^2}{2RB} \quad (\text{F.1})$$

$$h = H - R \cos \theta \quad (\text{F.2})$$

While Eq. (F.2) is intuitive, Eq. (F.1) is derived from the fact that $\frac{\delta}{\lambda} = \frac{\phi}{2\pi}$.

By differentiating Eqs. (F.1) and (F.2) with respect to the horizontal and vertical components of the baseline (B) respectively, we get

$$\delta h_{\text{horiz}} = \left(\frac{R}{B} \sin \theta \sin \alpha\right) \delta B_{\text{horiz}} \quad (\text{F.3})$$

$$\delta h_{\text{vertical}} = \left(\frac{R}{B} \sin \theta \cos \alpha\right) \delta B_{\text{vertical}} \quad (\text{F.4})$$

From Eqs. (F.3) and (F.4), the error in height measurements can be reduced by increasing the inter-satellite baseline (B). There is a tradeoff to be made, however, as longer baselines in the bistatic and multistatic cases result in signal decorrelation. The critical maximum baseline $B_{\text{crit-c}}$ defines the maximum separation of the receivers beyond which there is complete signal decorrelation, and the minimum baseline $B_{\text{crit-min}}$ defines the minimum separation of the receivers below which height errors in the resulting elevation measurement increase beyond a chosen acceptable level.

$$B_{\text{crit-c}} = \frac{2B_{\text{rg}}\lambda R \tan(\theta - \nu)}{c} \quad (\text{F.5})$$

$$B_{\text{crit-min}} = \frac{\lambda R \sin(\theta) \delta \phi}{2\pi \delta h} \quad (\text{F.6})$$

The critical baseline in Eq. (F.5) depends on the signal bandwidth B_{rg} , the wavelength, the range, the incidence angle, the local slope of the imaged terrain, and the speed of light c . The minimum baseline in Eq. (F.6) is determined by the wavelength, the range, the incidence angle, the interferometric phase error, and the maximum allowable height error in the elevation measurement h .

For our mission, the spacecraft system is at a 600 km orbital altitude (low Earth orbit) and the minimum detectable S/N (signal-to-noise ratio) used to calculate the interferometric phase error as shown in [1] is -12 dB (corresponding to existing SAR missions [2]) the values for $B_{\text{crit-c}}$ for four transmitter options shown.

The level of DEM accuracy can be determined using Eqs. (F.1) and (F.2) given the expected measurement capabilities of the spacecraft. Presuming a sub-centimeter baseline measurement accuracy, arcsecond attitude knowledge, and sub-degree phase measurement accuracy [3], the height error in the resulting DEMs will be on the order of one meter.

Current InSAR missions such as ERS, ENVISAT, Radarsat, JERS, and ALOS use data collected on multiple passes over a target area (multi-pass interferometry) to form digital elevation models, compared with single-pass interferometry, which uses multiple receivers to collect data in a single pass over the target area. Furthermore, multiple receivers can image the same terrain at short intervals, creating differential models of short time scale terrain changes.

Receiver spacecraft performing single-pass interferometry receive the same signal with a small time offset, eliminating the problem of changing terrain dynamics between multiple passes distorting

the resulting elevation models. This is especially important for our mission because ships and boats are constantly moving in the sea and this motion is mapped much better using a single-pass than a repeat-pass.

The spatial separation of the receivers also determines the nature of the data products and their applications. Cross-track baselines are used to generate terrain elevation data, while along-track baselines are used to map motion in the resulting images.

In other optical systems, the image obtained would not be able to detect precisely the coordinates of a ship within each pixel, especially when surveying a large area of ocean. High resolution optical instrument indeed obtain very good images of a particle target when detected over a small land area. However, when surveying huge expanses, it is not very easy to find multiple ships in the ocean. This problem is clearly eliminated using InSAR satellite systems.

Appendix G

Polarimetric interferometry

SAR interferometry has been successfully used to make a topographic map of the surface of the Earth. However, there is uncertainty as to whether the radar returns come from the actual ground surface or from a higher point such as the surface of a ship. By investigating the interferometric properties of the polarimetric data, vital information can be gained on where the scattering is coming from because the polarization signatures of the ship surface and the sea surface are quite different and can be separated using polarimetric data analysis. In the ideal case, information can be obtained on both the height of the surface and on the height of the ship, as well as parameters of the scattering volumes in between.

When two polarimetric images are obtained that satisfy the usual interferometric conditions of baseline and time lapse, the complete polarimetric/interferometric information is stored in three 3×3 complex matrices, the coherency matrix of each image, and the analogous matrix formed from the scattering vector of Image 1 times the scattering vector Image 2. Cloude and Papathanassiou [8] developed a phase-preserving polarimetric basis transformation that allows them to form interferograms between all possible elliptical polarization states. Then they develop an optimization procedure based on the singular value decomposition, which is used to find the polarization of Image 1 and the polarization of Image 2 that maximizes the interferometric coherence between the images. Most likely, the maximum coherence is obtained when the polarization of the two images is the same. The optimization finds polarizations that reduce the effect of baseline and temporal decorrelation. Nevertheless, if the temporal decorrelation is high, the procedure does not help significantly because the coherence will remain low independent of the polarization.

Furthermore, they develop a modified coherent target decomposition method, so that when combined with the coherence optimization procedure, the optimum scattering mechanisms can be found that lead to the best differential phase measurements (i.e. the highest coherence). The interferometric phase difference leads to the height difference between the physical scatterers possessing these mechanisms. The decomposition helps to understand the complex geometry of ships, by separating the return that comes from the upper and lower parts of the ship, or from the sea surface.

Appendix H

Applications and constraints of our unique flying formation

H.1 Digital Elevation Modeling

We have already shown that to improve the height accuracy of the target, the inter-satellite baseline needs to be large, but only up to the critical point, after which signal decorrelation would occur (see Eq. (F.5)).

Assuming a typical SAR radar, whose incidence angle varies from about 15° to 60° , we list some of the critical baselines needed for our satellite.

	$B_{\text{crit-c}}$ (km)			
Incidence angle ($^\circ$)	15	30	45	60
X-band	0.5	1.2	2.6	6.4

H.2 Superresolution

Forming superresolution imagery involves combining data from two or more images of the same location to produce a single image with a spatial resolution that is greater than that of the original imagery, and is useful for any application that requires a higher spatial resolution than is available from a given sensor, or if mission constraints such as cost, size, or power place a limit on the capabilities of an imaging sensor.

Superresolution imagery requires the length of the baseline between receivers be long enough such that the information in the received signals is independent, and cannot be combined to create interferograms. The distance at which this occurs separately defines a critical baseline for both the vertical and along-track directions. This new critical baseline for superresolution imagery occurs when the distance between receivers is long enough such that the path to each receiver from the same ground target has changed by more than a wavelength between each received pulse. Since the received signals are independent, they can be combined to form images with an improved azimuth or range resolution of up to a factor of two.

$$B_{\text{crit-c}} = \frac{\lambda}{D_p} \sqrt{R^2 + F^2} \quad (\text{H.1})$$

$$B_{\text{crit-v}} = \frac{2f_s \lambda R^2}{H_c c} \quad (\text{H.2})$$

	Along track baseline (km)				Vertical baseline (km)			
Incidence angle (°)	15	30	45	60	15	30	45	60
X-band	9.7	10.8	13.2	18.7	14.6	18.2	27.3	54.6

H.3 Moving object detection

If the along-track baseline is shorter than the critical baseline necessary for super-resolution imagery, the information received by both receivers is correlated and can be used to detect moving objects in the received images. Along-track interferometry uses the time delay between two receivers separated in the along-track direction to observe moving targets on the ground. The time delay δt seen between two receivers observing the same transmitted signal reflected off of the Earth is B_y/v_{plat} , or the along-track baseline divided by the platform velocity in the along-track direction. If δt is short compared to the signal decorrelation time, the observed phase difference between the two received signals can be used to determine the velocity of moving targets on the ground. The relationship between the observed phase ϕ , the wavelength λ , the along-track baseline and platform velocity, and the slant-range (cross-track direction) projection of the target velocity V_{ta} is shown in Eq. (H.4). V_{ta} is a function of the target velocities v_x and v_y in the cross-track and along-track directions, respectively, and the incidence angle θ , as shown

$$\phi = \frac{4\pi}{\lambda} \left(\frac{B_y}{v_{\text{plat}}} \right) v_{\text{ta}} \quad (\text{H.3})$$

$$v_{\text{ta}} = v_x \cos \theta - v_y \sin \theta \quad (\text{H.4})$$

Furthermore, since the measured phase ranges between zero and 2π , V_{ta} can be unambiguously measured only if the target moves less than $\pm\lambda/4$ within the time delay δt . This restriction provides a means of evaluating the suitability of different along-track baselines, incidence angles, and transmitter wavelengths for selected applications. In general, shorter along-track baselines allow higher target velocities to be observed, and a smaller incidence angle results in a higher V_{ta} .

	Maximum along the tract baseline (km)			
Incidence angle (°)	15	30	45	60
1 m/s target velocity	226	117	82	67
10 m/s target velocity	23	12	8	7
30 m/s target velocity	8	4	3	2

Appendix I

Imaging instrument trade-offs

I.1 High Resolution Optical Sensors

First, optical sensors are commonly used for high-resolution imagery of ground targets. However, some major limitations do exist. First, since optical sensors are passive, they rely on the light from the sun to illuminate the target. Hence, they are operational only in day time, which makes it unfavorable for maritime surveillance, especially because pirate attacks and accidents usually occur at night or in bad weather conditions. Moreover, cloud cover over Singapore is very frequent, preventing targets from being observed over a continuous period. Furthermore, although high resolution optical instruments can only focus on targets within a small range, when it comes to monitoring vast expanses of sea area, they are not very effective at spotting and tracking ships. Such wide range tracking can only be done using an SAR system.

I.2 Hyperspectral sensors

Similar to optical sensors, they can only be operated during the day. Moreover, their image resolution is much lower than our SAR system. The trade-off is that the power consumption is low, so the satellite size can be much smaller. However, since our mission's size limit is a total of 2000 kg, it is imperative that a SAR system should be used.

I.3 Real aperture radar

The resolution of a real aperture radar depends directly on the altitude of the satellite and inversely on the length of the radar antenna. At lower earth orbit altitudes and keeping the length of the antenna at a typical value, the resolution increases to the range of kilometers. To lower the resolution to 45 m, antenna length has to increase to the range of kilometers, which is not feasible.

I.4 Thermal infrared

Although it is possible to collect thermal infrared energy for ship detection and environmental monitoring, the instrument has to be kept at extremely low temperatures (approximately 75 K),

requiring cryogenics that will adversely affect the mass and power requirements of the thermal control subsystem. This would be very difficult for a small satellite.

I.5 Microwave remote sensing

Microwave remote sensing instruments work on the same principle as visible range cameras. The advantage of microwave is that the waves are able to pass through clouds. However, the resolution of microwave remote sensors is typically in the range of kilometers, which does not meet the requirements of our mission.

I.6 Single SAR satellite consisting of both transmitter and receiver in repeat-pass mode

The precision in height accuracy is only limited to stationary terrain for this system. A single SAR satellite uses a ‘repeat-pass’ mode to create the DEM, where the satellite notes the phase of the received radar echo from the specified target and revolves around the earth until it can get the phase of the second radar echo of that particular target. The phase difference is then analyzed to create the DEM. However, now suppose that the target is moving, such as a small ship vessel, at a speed of 20 knots. By the time the satellite orbits around the earth to take the second received radar echo phase, the target would have moved to a new location. This creates major inaccuracies in height variations of the ship and the sea, preventing accurate DEMs to be obtained.

Appendix J

Ship tracking using AIS and SAR imagery

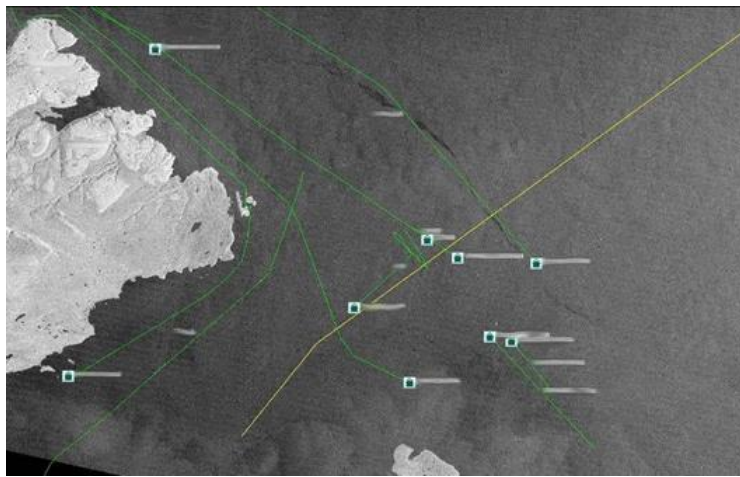


Figure 26: Tracking ships along the coast using AIS data with SAR imagery

Appendix K

Propulsion trade study

The main attraction for electric propulsion is the higher specific impulse, which, for the same ΔV , produces a more favorable mass fraction. This also equates to a lower fuel mass for electric than chemical propulsion, given a similar ΔV .

However, electric propulsion has significantly smaller thrust than chemical propulsion, meaning a much longer flight time for electric than chemical. This could become an issue if the electronics aren't properly shielded from radiation. On the other hand, the cost for electric propulsion is much lower than chemical propulsion. The cost of the electric thruster built in the MIT SPL is about \$4000, and the Xenon fuel is projected to cost on the order of \$50 000. However, according to Dr. Martinez-Sanchez from MIT SPL, the cost of a chemical rocket would be on the order of \$1 000 000, which is about twenty times the expected cost of the electrical system.

Furthermore, there is the concern of having three separate satellites due to our requirement for a unique cluster flying formation for our SAR subsystem to function. This means we will have up to three different chemical propulsion systems, any of which are relatively more dangerous than the electrical alternative. However, we do recognize that chemical thrusters have been used extensively in the past and have a history of exceptional performance.

From an orbit maintenance and de-orbit standpoint, because the main portion of the fuel is only required at the final stage of decommissioning the satellite, it will mean that the moment of inertia and associated parameters are greater for the satellite during most of its flight, in the case of choosing a chemical propulsion system. This also means that our reaction wheels, cold gas thrusters and other associated attitude control subsystem components will require more fuel/mass, which is more costly.

In conclusion, we chose the Hall-effect thrusters over the chemical propulsion systems due to concerns over safety, and due to mass and cost considerations.

The electronic propulsion subsystem will run off the solar arrays in sunlit portions of the trajectory and the batteries in the shadow portion. The use of payload battery power for electric propulsion is described in the power subsystem section.

Propulsion type	Thruster mass/kg	Flight time (deorbit)	Cost	Thrust	I_{sp}/s	m_f/m_i
Electric	2.064	2 mths to 3 mths	\$4000 + \$50 000	13.4 mN	1640	0.763
Chemical	10.323	2 mths to 3 mths	\$1 000 000	400 N	300	0.277

Appendix L

Hall effect thruster

Hall effect thrusters work by creating and accelerating a plasma beam or plume. This is done by creating a flow of free electrons from an external cathode which travel into the thruster due to the electric field created by the thruster anode. The electrons are then trapped in orbits by a magnetic field created in the thruster and the aforementioned electric field. When the propellant flows through these orbits, the gas molecules collide with the electrons and the high-energy collisions ionize the gas. Being much more massive than the electrons, the ionized gas is accelerated by the electric field and leaves the thruster at high speed. This particular Hall thruster uses a diverging channel with an anode at the upstream center and cusped magnetic fields created by three permanent samarium cobalt magnets surrounding the conical diverging channel. This design aims to decrease the damage to both the channel and the anode from collisions with the charged particles inside the channel. The decreased rate of damage allows for longer operation as the limiting factor in thruster lifespan is the erosion and damage of the channel wall insulator (needed to protect the magnets from heat) and the anode itself.

From the data analysis by Dan Courtney, the first DCHT reaches a peak power/thermal efficiency of 44.5% and 1641 s. This produces a thrust of 13.4 mN. These are in line with trade studies of other commercial 200 W-class Hall thrusters. Because the efficiency is comparable to other 200 W thrusters and the I_{sp} and thrust values are within the design ranges, this fulfills the requirements for our orbital maintenance and de-orbit maneuvers.

Furthermore, the original DCHT was designed to reduce the erosion of the insulating boron nitride cone by the ion plume using the cusped magnetic fields. This should lead to a longer lifespan than similar Hall thrusters. Considering the fact that our LEO satellite orbit will require both cyclical and constant thrusting to maintain the high accuracy of orbit for the SAR/ASAR subsystems to work, this will fulfill the requirement of an accurate propulsion system for orbit maintenance. Finally, the cathode used on the original DCHT can be heated in approximately 5 minutes and the thruster will otherwise require little or no power when not operating, fulfilling the final requirement for a cyclical orbit maintenance, as suggested by Larson and Wertz [36, ch. 11.1] for our satellite requirements.

Appendix M

Attitude Sensors

M.1 Star sensor

Due to the high precision and accuracy required by the SAR to generate high resolution images, star sensors are used to measure attitude. However, because the star sensors are too slow to control a spacecraft's response, Larson and Wertz [36] recommends coupling these with gyroscopes for high accuracy and rapid response. Conversely, because gyroscope accuracy is limited by instrument drift, most gyroscope systems are used in conjunction with an absolute reference, which in our case is the star sensor. In effect, these two systems complement each other.

M.2 Sun sensor

A sun sensor will be mounted on the end of each solar array pointing away from the main vehicle. By rotating the solar panels to sense the sun (by checking if power is being output) in any direction normal to their axis and using the sun sensors along this axis, the sun will be located in any orientation. The vehicle will not have a line of sight to the sun during eclipse and therefore, the sun sensors will not be used during eclipse.

The sun sensors consist of four photodiodes (two in the x -axis, two in the y -axis) that detect the patch of direct sunlight that passes through an entrance aperture and use this measurement to determine the position of the sun. The sensors will use approximately 2 W of power each and weigh approximately 40 g.

M.3 Rate gyros

The vehicle will contain two tri-axis solid state rate gyros (one for redundancy) that will continually track the rotation rate of the vehicle. The rate gyros are sensitive to drift in their measurement accuracy over time and will require a true attitude update every half a minute from the star sensor. The rate gyros can be purchased from an outside vendor. (Analog Devices sells several different types of rate gyros, ranging from \$30 to \$600. The two rate gyros combined will weigh less than 0.1 kg and draw less than 2 W of steady power.)

M.4 Actuators

The design uses twelve N_2 thrusters for attitude control. Compressed gas was used because liquid propellant thrusters are dangerous to use and too complicated to manufacture. Nitrogen gas was selected because it is low-cost, readily available, safe and has a high I_{sp} (65 to 70) relative to other gas options.

The thrusters will be aligned to provide control in all three axes. Two sets of opposite pointing thrusters will be placed on opposite sides of the vehicle in each of the axes. In this configuration, the thrusters can successfully point the thruster, solar panels, and antennas (although antennas and solar panels cannot be pointed perfectly at all times because each requires a different roll orientation). The N_2 will be stored in an aluminum tank.

M.5 Engine gimbal

The major internal torque that the vehicle must overcome will occur when the Hall thruster (main engine, only during required LEO orbit insertion from deployment from ariane5 launch vehicle) is not firing through the center of mass. The center of mass will change during the orbit transfer based on the mass of fuel in the tanks changing as the fuel is used. If the engine is firing on a vector that does not go through the center of mass, then the engine will create torques on the vehicle that will require a significant mass of propellant to overcome. To solve this problem, the engine will be gimballed so that its direction can be continuously changed to fire through the center of mass during the mission.

M.6 Antenna gimbal

To reduce the antenna pointing requirements for the ADCS subsystem, the antenna will be attached to a gimbaling mechanism that will allow the antenna (AIS, 406 MHz antenna, SAR, communications) to point separately from the vehicle. The antenna sends signals to the earth via telemetry.

Appendix N

Hill equations

Hill equations (also known as Clohessy-Whitshire equations) are a set of differential equations to calculate the relative motion of the satellites taking into account the Earth.

$$\ddot{r} - r\dot{\theta}^2 - r\dot{\phi}^2 + \frac{\mu}{r^2} = 0 \quad (\text{N.1})$$

$$r\ddot{\theta} \cos \phi + 2\dot{r}\dot{\theta} \cos \phi - 2r\dot{\theta}\dot{\phi} \sin \phi = 0 \quad (\text{N.2})$$

$$r\ddot{\phi} + 2\dot{r}\dot{\phi} + r\dot{\theta}^2 \sin \phi \cos \phi = 0 \quad (\text{N.3})$$

Note that the above equations are a sixth-order system of coupled, nonlinear ordinary differential equations. An exact solution of these equations is not possible, hence the need to introduce techniques that can be used to find approximate solutions.

We used the STK software to accurately map out the relative baselines using the software's numerical approach.

Appendix O

Integration of SAR images

The SAR sensor transforms object spectra to data spectra. The data frequency resulting from a certain object frequency depends on the incidence angle and direction of the SAR signal. As the two SAR images used to generate the interferogram are taken with (slightly) different incidence angles, an object frequency is belonging to different frequencies in the data spectra. As the SAR sensor images only those object frequencies which are located in the sensor-specific frequency band, both data spectra contain partially different, in the object spectra non-overlapping object information.

By common-band filtering those non-overlapping frequency bands are filtered out from both SAR images. This limits the information used for interferogram generation to the frequency bands containing the same object information (Gatelli et al. [18], Geudtner [20]). After common-band filtering, the images are coregistered with sub-pixel accuracy e.g. with an accuracy of 0.1 pixels. As the imaging geometries of both images are—in comparison with stereo photogrammetry—very similar, fulfilling this requirement is usually easy. Then the second SAR image is resampled in the geometry of the first one using a suitable interpolation method such as Shannon or bi-cubic polynomial interpolation. When both SAR images resemble the same geometry and contain completely overlapping object spectra, the interferogram is computed according to

$$I = V_1 V_2^* = |V_1| |V_2| e^{i\phi} \quad (\text{O.1})$$

where $\phi = \varphi_1 - \varphi_2$ is the interferometric phase, V_1 is the complex signal (amplitude and phase) of image 1 (master), and V_2 is the complex signal of image 2 (slave), and * indicates complex conjugation. A final interferogram is computed by subtracting a simulated interferogram e.g. the interferogram of a tangential plane to the geoid, the so-called flat earth, from the measured interferogram.

Appendix P

Operating area and spatial resolution calculations

P.1 Operating area

The bi-static radar equation is given by

$$(R_t R_r)^2 = \frac{P_t G_t G_r \lambda^2 \sigma_B F_t^2 F_r^2}{(4\pi)^3 k T_s B_n (S/N) L_t L_r} \quad (\text{P.1})$$

where

- R_t and R_r are the ranges from the ground target to the transmitter and receiver, respectively.
- P_t is the transmitter power.
- G_t and G_r are the gains of the transmit and receive antennas respectively.
- λ is the signal wavelength.
- σ_B is the bistatic radar cross-section of the target.
- F_t and F_r are the atmospheric pattern propagation factors between the target and the antennas.
- k is the Boltzmann's constant.
- T_s is the receiver noise temperature.
- B_n is the noise bandwidth of the receiver.
- S/N is the minimum detectable signal-to-noise ratio.
- L_t and L_r are system losses that are not included in the other parameters.

The operating range of a bistatic configuration is determined by the intersection of a maximum constant range sum contour, and an “oval of Cassini”—a representation of noise-limited signal detection contours. For the purpose of simplification, K is defined as the bistatic constant:

$$K = \frac{P_t G_t G_r \lambda^2 \sigma_B F_t^2 F_r^2}{(4\pi)^3 k T_s B_n L_t L_r} \quad (\text{P.2})$$

The bistatic radar equation is rearranged in order to plot the minimum signal-to-noise ratio, and re-written as Eq. (P.4) with R_t and R_r being the range to a ground target in polar coordinates to plot an oval of Cassini. The maximum range contour for each given S/N is an ellipse defined in Eq. (P.5).

$$S/N = \frac{K}{R_t^2 R_r^2} \quad (\text{P.3})$$

$$S/N = \frac{K}{\left(r^2 + \frac{L^2}{4}\right)^2 - r^2 L^2 \cos^2 \theta} \quad (\text{P.4})$$

$$(R_t R_r)_{\max} = \sqrt{\frac{K}{S/N}} \quad (\text{P.5})$$

Thus, for a given following distance between transmitter and receiver, bistatic constant K , and minimum detectable S/N , the operating region of the bistatic radar configuration is defined by the corresponding maximum range contour and oval of Cassini. Additionally, the operating area of a given bistatic pair is constrained by the incidence angle of the sensors, which commonly falls within the 15° to 60° range.

P.2 Spatial Resolution

The range and azimuth spatial resolutions, determined by the orbital frame of reference defined in Figure 12, available in each received image are calculated separately for each bistatic pair (transmitter/receiver pair). The resolutions are determined by the geometry of the pair, as well as the radar pulse width and the Doppler resolution.

The equations for the range resolution α_r and azimuth resolution α_a follow in Eq. (P.1) and Eq. (P.4). The angle between the range vectors from the target to the transmitter and receiver (β) is the bistatic angle; τ is the time width of the radar pulse; T is the integration time; V_t and V_r are the velocities of the transmitter and receiver; R_t and R_r are the ranges from the transmitter and receiver to the ground target; and α_t and α_r are the angles between the transmitter-to-target or receiver-to-target line of sight vector and the velocity vector.

$$\delta_r = \frac{c\tau}{2 \cos(\beta/2)} \quad (\text{P.6})$$

$$\delta_a = \frac{\lambda}{T \cos(\beta/2)} \left| \frac{V_t \sin \alpha_t}{R_t} + \frac{V_r \sin \alpha_r}{R_r} \right|^{-1} \quad (\text{P.7})$$

The range resolution varies with the bistatic angle, and therefore the “following distance” between the transmitting satellite and the receiving satellite. The cross-range resolution varies with the chosen wavelength, the following distance, the integration time, the speed of the platforms, and the following distance between the transmitter and the receiver. The integration time is determined by

the processing done onboard the receiver satellite, and can vary depending on how much processing power and time is available. For the purpose of this investigation, a typical SAR 0.8 second integration time was used.

Appendix Q

Power subsystem

Q.1 Eclipse time calculation

For an orbit to have no eclipse, the maximum inclination β_{\max} with respect to the ecliptic plane (see Figure 27) is given by $\beta_{\max} = \arcsin\left(\frac{1}{1+\frac{h}{R_0}}\right)$ where $h = 610$ km is the orbit altitude and $R_0 = 6371$ km is the mean Earth radius. Since our orbit inclination is $\beta = 23.5^\circ$, the maximum eclipse period is

$$T_n = \frac{P}{180} \arccos\left(\frac{\cos \beta_{\max}}{\cos \beta}\right) \approx 38 \text{ mins} \quad (\text{Q.1})$$

where $P = 103$ mins is the period.

Q.2 Solar array sizing calculations

Q.2.a Main satellite

The satellite is over Singapore at most once per period for a duration of $T_{\text{Singapore}} \approx 7$ minutes 10 seconds. Since the period is $T = 103$ minutes and the maximum eclipse time is $T_{\text{eclipse}} \approx 38$ minutes, the minimum time in sunlight is $T_{\text{sunlight}} = 65$ minutes. All energy consumed in a daylight-eclipse cycle has to be produced by the solar array. For analysis, one period with the satellite over Singapore

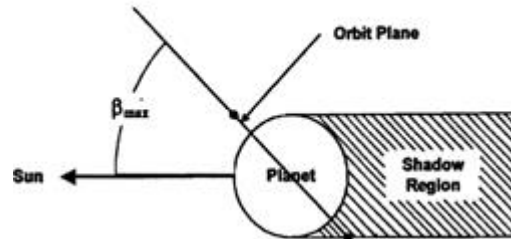


Figure 27: Maximum β angle for an eclipse-free period (Brown [5])

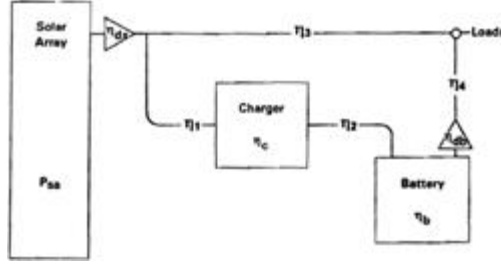


Figure 28: Sources of power losses in a DET (Direct Energy Transfer) system

during eclipse is chosen for evaluation. Thus the total power output of the solar array P_{sa} is given by

$$P_{sa} \times T_{sunlight} = \frac{P_{eclipse} T_{eclipse, Spore} + P_{eclipse, others} T_{eclipse, others}}{X_{ab} X_{bl}} + \frac{P_{sunlight} T_{sunlight}}{X_{al}} \approx 1104 \text{ W} \quad (\text{Q.2})$$

where

- The power transfer efficiency from the solar array to the battery is $X_{ab} \approx 0.80$.
- The power transfer efficiency from the battery to the loads is $X_{bl} \approx 0.95$.
- The power transfer efficiency from the solar array to the loads directly is $X_{al} \approx 0.90$.
- The power consumption during eclipse over Singapore is $P_{eclipse, Spore} \approx 5350 \text{ W}$.
- The power consumption during eclipse over other areas is $P_{eclipse, others} \approx 189 \text{ W}$.
- The power consumption during sunlight over other areas is $P_{sunlight} \approx 189 \text{ W}$.

The various sources of power losses in a DET (Direct Energy Transfer) system are illustrated in Figure 28 where

- η_1 , η_2 , η_3 and η_4 are the power transfer efficiencies in the power cables.
- η_c is the charger efficiency.
- η_b is the battery charging efficiency.

The realistic power output of each triple-junction GaAs solar cell P_{cell} is given by Brown [5, p.343]:

$$P_{cell} P_L \eta_{rad} \eta_{UV} \eta_s \eta_{cy} \eta_m \eta_t \eta_{con} \eta_r L_p = 0.943 \text{ W} \quad (\text{Q.3})$$

where

- The maximum power output of one cell in ideal laboratory condition (28°C , no radiation) is $P_L = 1.169 \text{ W}$.
- The power loss due to radiation damage after 5 years when subjected to an equivalent 1 MeV total radiation dose of $5 \times 10^4 \text{ e/cm}^2$ in orbit is $\eta_{rad} = 0.971$.

- The power loss due to UV discoloration of cell materials (darkening of cover glass slide and adhesive) is $\eta_{UV} \approx 0.98$.
- The power loss due to the shadowing of solar cells by satellite appendages is $\eta_s \approx 0.98$ as shadowing is minimal for our satellite.
- The power loss due to thermal cycling is $\eta_{cy} \approx 0.99$.
- The power loss due to cell mismatch is $\eta_m \approx 0.975$.
- The power adjustment for operating temperature is $n_t = 1 - (100 - 28) \times 0.00064 = 0.954$ assuming hottest temperature of 100°C after a full Sun period.
- The power loss due to contamination from all sources is $\eta_{con} \approx 0.98$.
- The power loss due to resistance in cell interconnection is $\eta_r = 0.98$.
- The array pointing loss factor is $L_p = \cos 1.3^\circ = 0.999$ as the Sun pointing accuracy of our solar array actuating mechanism is within 1.3° .

Allowing for a margin of 20%, the approximate area of the array is given by

$$A_{sa} = \frac{P_{sa} \times A_{cell}}{P_{cell} \times D \times \text{margin}} = 4.42 \text{ m}^2 \quad (\text{Q.4})$$

where

- The area of one solar cell is $A_{cell} = 26.6 \text{ cm}^2$.
- The packing factor is $D \approx 0.88$.

With an area density of 84 mg/cm^2 , the mass of the solar array is approximately 3.71 kg .

Q.2.b Trailing satellite

By similar calculations, the total power output from the solar array is 430 W and the required area is 1.72 m^2 .

Q.3 Primary battery

The maximum combined time duration of both phase 2 and 7 is approximately 45 minutes. The required battery's watt-hour capacity of the main satellite, with a 20% margin, is 1000 Wh . The battery's mass is approximately 3 kg . For the trailing satellite, the capacity is 830 Wh with mass of 2.4 kg .

Q.4 Secondary battery

To achieve a battery lifetime of 5 years or 30 000 cycles of charge and discharge, the depth of discharge (DOD) is set at maximum 40%. Allowing for a margin of 20%, the battery's watt-hour capacity for the main satellite is given by

$$E = \frac{P_{\text{eclipse,Spore}}T_{\text{eclipse,Spore}} + P_{\text{eclipse,others}}T_{\text{eclipse,others}}}{X_{\text{bl}} \times DOD \times \text{margin}} = 2150 \text{ Wh} \quad (\text{Q.5})$$

With a specific energy of 175 Wh/kg, the battery has mass 12.3 kg. The battery of each trailing satellite has capacity 560 Wh and mass 3.2 kg.

Appendix R

Thermal subsystem

First-order estimates of the satellite thermal performance can be made by assuming an isothermal and spherical spacecraft with surface area 10 m^2 . A sphere with the same surface area will have a diameter of 0.892 m . We assume the surface is covered with aluminized Teflon with EOL solar absorptivity $\alpha_s = 0.316$ and IR emissivity $\varepsilon = 0.8$.

	Worst case hot	Worst case cold
Solar constant	1414 W/m^2	1322 W/m^2
Albedo at orbital altitude	0.28	0.18
Radiator solar absorptivity	0.11	0.09
Earth IR emission intensity	275 W/m^2	228 W/m^2
Power dissipation	238 W	145 W

The satellite's worst case hot temperature is given by

$$T_{\text{MAX-S}} = \left[\frac{\frac{G_s \alpha_s}{4} + q_{\text{IR}} \varepsilon_{\text{IR}} F_{\text{s-e}} + G_s \alpha \alpha_s K_a F_{\text{s-e}} + \frac{Q_w}{\pi D^2}}{\sigma \varepsilon_{\text{IR}}} \right]^{1/4} = 290 \text{ K} = 17^\circ \text{C} \quad (\text{R.1})$$

where

- The maximum solar constant is $G_s = 1414 \text{ W/m}^2$.
- The sphere's EOL surface emission absorptivity is $\alpha_s = 0.316$.
- The maximum Earth IR emission intensity is $q_{\text{IR}} = 275 \text{ W/m}^2$.
- The sphere's surface IR emissivity is $\varepsilon_{\text{IR}} = 0.8$.
- The view factor, Sun to Earth, is $F_{\text{s-e}} = 0.5 \left[1 - \frac{(H^2 + 2HR_E)^{0.5}}{H + R_E} \right] = 0.332$.
- The Earth's maximum albedo is $\alpha = 0.28$.
- The factor to account for the reflection of collimated incoming solar energy off a spherical Earth is

$$K_a = 0.657 + 0.54 \frac{R_E}{R_E + H} - 0.196 \left(\frac{R_E}{R_E + H} \right)^2 = 0.972 \quad (\text{R.2})$$

- The maximum heat dissipation is $Q_W = 238 \text{ W}$.
- The diameter of the spherical satellite is $D = 0.892$.
- The Boltzman constant is $\sigma = 5.67 \times 10^{-8} \text{ W/m}^2\text{K}^4$.

Since the worst case hot temperature $T_{\text{MAX-S}}$ is below the maximum operating temperature of all equipment, a body-mounted radiator can be used.

The worst case cold temperature is

$$T_{\text{MIN-S}} = \left[\frac{q_{\text{IR}}\varepsilon_{\text{IR}}F_{\text{s-e}} + \frac{Q_w}{\pi D^2}}{\sigma\varepsilon_{\text{IR}}} \right]^{1/4} = 226 \text{ K} = -47^\circ\text{C} \quad (\text{R.3})$$

where

- The Earth's minimum IR emission intensity is $q_{\text{IR}} = 228 \text{ W/m}^2$.
- The sphere's surface IR emmissitivity is $\varepsilon_{\text{IR}} = 0.8$.
- The view factor, Sun to Earth, is $F_{\text{s-e}} = 0.5 \left[1 - \frac{(H^2 + 2HR_E)^{0.5}}{H + R_E} \right] = 0.332$.
- The Earth's minimum albedo is $\alpha = 0.18$.
- The factor to account for the reflection of collimated incoming solar energy off a spherical Earth is

$$K_a = 0.657 + 0.54 \frac{R_E}{R_E + H} - 0.196 \left(\frac{R_E}{R_E + H} \right)^2 = 0.972 \quad (\text{R.4})$$

- The minimum heat dissipation is $Q_W = 145 \text{ W}$.
- The diameter of the spherical satellite is $D = 0.892$.
- The Boltzman constant is $\sigma = 5.67 \times 10^{-8} \text{ W/m}^2\text{K}^4$.

Using a Optical Solar Reflector (OSR) 8 mil quartz mirror with EOL $\alpha = 0.11$ and $\varepsilon_{\text{IR}} = 0.80$ as radiator surface finish to keep the equipment at a safe temperature of 20°C , the required radiator area A_R is given by

$$G_s\alpha_s A_R + q_{\text{IR}}F_{\text{a-e}}\varepsilon_{\text{IR}}A_R + G_s\alpha F_{\text{a-e}}\alpha_s K_a A_R + Q_W = A\sigma\varepsilon T^4 \quad (\text{R.5})$$

where

- The maximum solar constant is $G_s = 1414 \text{ W/m}^2$.
- The radiator EOL surface solar absorptivity is $\alpha_s = 0.11$.
- The maximum heat dissipation is $Q_W = 238 \text{ W}$.
- The Boltzman constant is $\sigma = 5.67 \times 10^{-8} \text{ W/m}^2\text{K}^4$.
- The surface IR emissitivity is $\varepsilon_{\text{IR}} = 0.8$.

- The Earth's maximum IR emission intensity is $q_{\text{IR}} = 275 \text{ W/m}^2$.
- The radiator temperature is $T = 20^\circ\text{C} = 293 \text{ K}$.
- The radiation view factor radiator to Earth is $F_{\text{a-e}} = \frac{R_{\text{E}}^2}{(H+R_{\text{E}})^2} = 0.912$.
- The Earth's maximum albedo is $\alpha = 0.28$.
- The factor to account for reflection of collimated incoming solar energy off a spherical Earth is $K_a = 0.972$.

This yields radiator area $A_{\text{R}} = 1.5 \text{ m}^2$.

The temperature of the radiator under worst case cold condition is given by

$$q_{\text{IR}}F_{\text{a-e}}\varepsilon I R A_{\text{R}} + Q_{\text{W}} = A\sigma\varepsilon T^4 \quad (\text{R.6})$$

where

- The minimum heat dissipation is $Q_{\text{W}} = 238 \text{ W}$.
- The Boltzman constant is $\sigma = 5.67 \times 10^{-8} \text{ W/m}^2\text{K}^4$.
- The surface IR emissivity is $\varepsilon_{\text{IR}} = 0.8$.
- The radiator area is $A_{\text{R}} = 1.5 \text{ m}^2$.
- The Earth's minimum IR emission intensity is $q_{\text{IR}} = 228 \text{ W/m}^2$.
- The radiation view factor radiator to Earth is $F_{\text{a-e}} = \frac{R_{\text{E}}^2}{(H+R_{\text{E}})^2} = 0.912$.
- The factor to account for reflection of collimated incoming solar energy off a spherical Earth is $K_a = 0.972$.

which yields a radiator temperature of $T_{\text{MIN-S}} = 274 \text{ K} = 1^\circ\text{C}$. This is also within the operating temperature range of all equipments but to allow for a safe thermal margin of 10°C , heaters with total power of 10 W will still be provided in case of a dramatic temperature drop. The radiator will also be fitted with louvers which reduce heat dissipation from the radiator up to five or six times (at 238 K at fully closed, the heat rejection rate is only 54 W/m^2 , compared to 430 W/m^2 at 304 K and fully open) depending on radiator temperature.

By similar calculations, the microsatellite each requires 1 m^2 of radiator area.

Appendix S

Antenna calculation

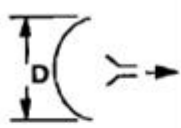
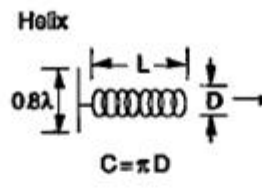
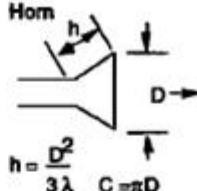
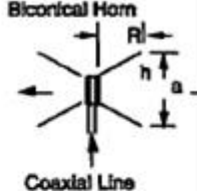
Antenna Type	Parabolic Reflector	Helix	Horn	Biconical Horn
				
Beam Shape	Conical	Conical	Conical	Toroidal
Typical Max Gain (dBi)	15–65	5–20	5–20	0–5
Peak Gain (dBi)	$17.8 + 20 \log D + 20 \log f$ ($\eta = 0.55$)	$10.3 + 10 \log (C^2 L / \lambda^3)$ $0.8 \leq C / \lambda \leq 1.2$ ($\eta = 0.70$)	$20 \log (C / \lambda) - 2.8$ ($\eta = 0.52$)	$5 \log (h / \lambda) + 3.5$ $R > 2\lambda$ $\alpha = P(2\eta\lambda)$
Half-Power Beamwidth (deg)	$\frac{21}{fD}$	$\frac{52}{\sqrt{C^2 L / \lambda^3}}$	$\approx \frac{225}{(C / \lambda)}$	Typically $40^\circ \times 360^\circ$ for gain ≥ -1 dBi $70^\circ \times 360^\circ$ for gain ≥ -3 dBi
Peak Gain & Dimensions of 18° Beam at 400 MHz	$G = 19.1$ dBi $D = 2.9$ m	$G = 19.5$ dBi $D: 0.19$ m 0.24 m or $L: 9.8$ m 6.2 m	$G = 19.1$ dBi $D = 3$ m $h = 4$ m	—

Figure 29: Antenna dimension calculation from Larson and Wertz [36]

Appendix T

Optical/laser trade study

Optical/laser terminals are a promising alternative for intersatellite communication as they are able to provide clean, focused with high data rate transfer at lower weight.

Typical saser source and wavelength for intersatellite link (in μm):

- Diode pumped Nd YAG (YAG): 1.064 to 0.503
- Indium Gallium Arsenide Phosphide (InGaAsP): 1.3 to 1.5
- Aluminum Gallium Asenide (AlGaAs): 0.8

See Figures 30 and 31.

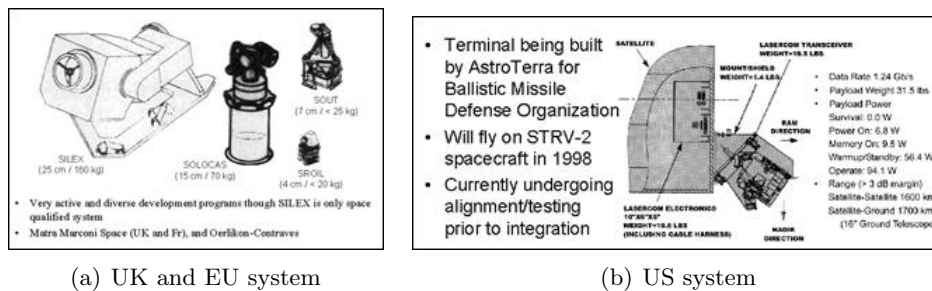


Figure 30: Two kinds of systems

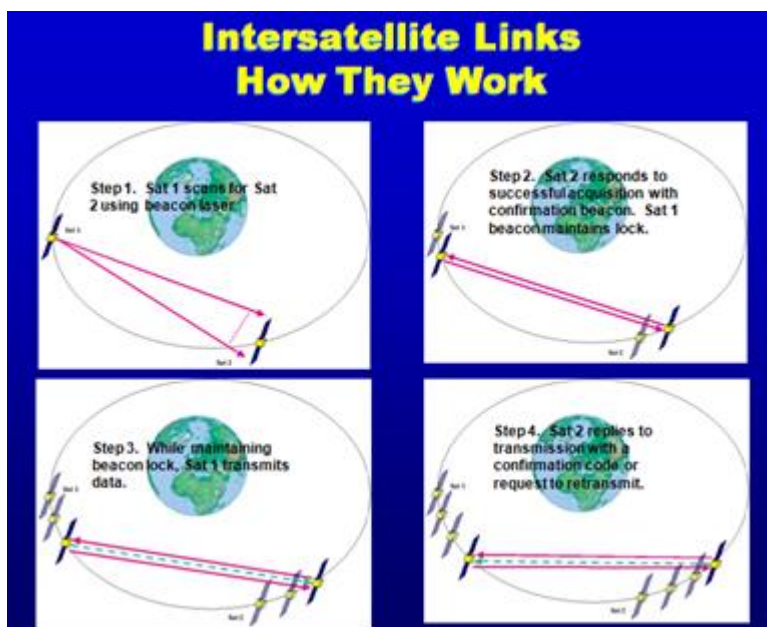


Figure 31: Intersatellite link using lasers

Appendix U

Deployment mechanism

U.1 Launch vehicle detachment

For the trailing microsattellites with the main function of SAR/ASAR communications, they will be attached to the ASAP adapter while the main satellite will be fitted with the options provided by Arianespace. We are unable to make an informed decision as of this moment because their user manual provided to us did not include a finalized version of mass and center of gravity curve used for selecting the payload adapter. However, it is understood that the adapters will include either pneumatic or spring-based actuators to separate the payload from the launch vehicle. For redundancy, we will add an additional spring-based deployment mechanism for separation in case the primary pneumatic actuator provided fails (in any case, we will still deploy the secondary spring-based component as it is not useful). The ADCS will then take over for the main satellite and separate from the payload adapter and launch vehicle components.

For the trailing satellites, because the ASAP adapter does not include a similar pneumatic actuator to separate the satellite from the ASAP adapter, we will rely on a spring-based mechanism to separate from the adapter, and also an explosive bolt configuration for redundancy, in case the spring based deployment mechanism fails to detach. The ADCS and hall effect thruster will then push the main body away from the remains of the launch vehicle to its intended orbit.

U.2 Solar array drive

The solar arrays wrap around the vehicle during launch, with one panel forming each side of a box. They are secured in place using Dyneema wire under pretension. Dyneema is a polymer wire that is stronger than Nylon but melts at a lower temperature (150 °C). To break the wire, two small redundant resistors on each wire will melt through the wire. When released from vehicle, torsion springs will unfold the panels, and damping mechanisms will critically damp the panels' motion such that they can get into place when they reach $\pm 180^\circ$. There will be no locks in case they damage the solar panels.

Having extra explosive bolts to detach the wires from the main body can prevent the solar panels from not being able to deploy due to one reason or another. If that fails, the solar panels are still put facing outwards, which can guarantee some sunlight still being collected to feed the battery system.

In that case, we can cut power to subsystems such as the SAR or the COSPAS SARSAT in order to use it for the other subsystems which is more important to our customer's mission.

U.3 Antenna

The passive receiver SAR antenna used in our mission's trailing satellites will be stowed in a folded configuration for both satellites, and when deployed, will be unfurled by releasing pins to the catches that keep the antenna in its stowed position. An electric motor will then draw the mast out from the stowed configuration, and be used to stretch the parabolic dish from its stowed configuration.

The rest of the antennas are connected to bi-axial gimbals, and therefore will be stowed close to the main body and then, by mechanical movements of the gimbal arms, deploy to their intended positions around the satellite.

U.4 SAR (main satellite)

Due to the relatively large size of the SAR antenna to the main satellite, we will adopt a folded configuration (4 times) for the SAR satellite such that it is stowed beneath the solar array before deployment. It will be deployed only when the solar arrays are confirmed to have deployed via telemetry data received on the ground.

The deployment of these SAR antenna parts will be done in a similar fashion to the solar array with a torsion spring mechanism and Dyneema wires holding them in the stowed configuration. Dampers will be used to minimize any unwanted mechanical vibrations due to the deployment, and mechanical latches will hold the SAR antenna in place once full deployment is reached. The gimbaling mechanism will then adjust its position to the required nadir pointing direction it requires to function.

U.5 Cable antenna

For the deployment of the cable antenna, we will utilize a long tape spring wound in a confined box. A microswitch will be used to activate two small redundant resistors on each wire that will melt through the Dyneema wire that holds the tape spring in the confined box.

Appendix V

Link budget

See Tables 27 to 29.

Item	Unit	Value
Uplink frequency	GHz	8
Uplink transmitting antenna diameter	m	6.5
Uplink antenna aperture efficiency		0.65
Transmitting forward power	dBW	20
Range	km	600
Bandwidth	KHz	1
Uplink antenna gain	dBi	52.85
Uplink EIRP	dBW	72.85
Uplink path loss	dB	166.07
Uplink C/N	dB	719.37

Table 27: Uplink calculation

Item	Unit	Value
Downlink frequency	GHz	7.5
Downlink receive antenna diameter	m	6.5
Downlink receive antenna efficiency		0.65
System noise temperature	dBK	21
Weather margin	dB	3
Receive antenna gain	dBi	52.29
Receive antenna G/T	dB/K	31.29
Downlink path loss	dB	165.51
Downlink C/N	dB/Hz	104.88

Table 28: Downlink calculation

Item	Unit	Value
Satellite G/T	dB/K	614
Satellite EIRP	dBW	37.51
Satellite range	km	60
Satellite PFD	dBW/m ²	-53.7
Uplink C/N	dB/Hz	719.37
Downlink C/N	dB/Hz	104.88

Table 29: Satellite link summary

Bibliography

- [1] R. Bamler, N. Adam, G. W. Davidson, and D. Just, “Noise-induced slope distortion in 2-d phase unwrapping by linear estimators with application to sar interferometry,” *IEEE Transactions on Geoscience and Remote Sensing*, vol. 36, no. 3, pp. 913–921, 1998.
- [2] R. Bamler, D. Geudtner, B. Schattler, P. Vachon, U. Steinbrecher, J. Holzner, J. Mittermayer, H. Breit, and A. Moreira, “Radarsat scansar interferometry,” in *Geoscience and Remote Sensing Symposium, 1999. IGARSS '99 Proceedings. IEEE 1999 International*, vol. 3, 1999, pp. 1517–1521 vol.3.
- [3] R. Bamler and P. Hartl, “Synthetic aperture radar interferometry,” *Inverse Problems*, vol. 14, no. 4, pp. R1–R54, 1998.
- [4] W.-M. Boerner, “Recent advances in radar polarimetry and polarimetric sar interferometry,” in *Radar Polarimetry and Interferometry*, ser. RTO Educational Notes. RTO/NATO, 2005, ch. 8.
- [5] C. D. Brown, *Elements of Spacecraft Design*, ser. AIAA Education Series. American Institute of Aeronautics and Astronautics, 2002.
- [6] R. Burns, C. A. McLaughlin, J. Leitner, and M. Martin, “Techsat21: Formation design, control and simulation,” in *Aerospace Conference Proceedings*, 2000.
- [7] J. Chen, Y. Zhou, and C. Li, “Formation flying orbit design for the distributed synthetic aperture radar satellite,” *Science in China Series F: Information Sciences*, vol. 47, no. 6, pp. 741–751, 2004. [Online]. Available: <http://dx.doi.org/10.1360/03yf0210>
- [8] S. R. Cloude and K. P. Papathanassiou, “Polarimetric sar interferometry,” *IEEE Transactions on Geoscience and Remote Sensing*, vol. 36, no. 5, pp. 1551–1565, 1998.
- [9] S. Cloude and E. Pottier, “A review of target decomposition theorems in radar polarimetry,” *Geoscience and Remote Sensing, IEEE Transactions on*, vol. 34, no. 2, pp. 498–518, Mar 1996.
- [10] M. Costantini, “A novel phase unwrapping method based on network programming,” *IEEE Transactions on Geoscience and Remote Sensing*, vol. 36, no. 3, pp. 813–821, 1998.
- [11] M. Crosetto, “Interferometric sar for dem generation: Validation of an integrated procedure based on multisource data,” Ph.D. dissertation, Politecnico di Milano, Geodetic and Surveying Sciences, Milano, 1998.

- [12] A. Das and R. Cobb, "Techsat 21 - space missions using collaborating constellations of satellites," *Proceedings of the 12th AIAA/USU Annual Conference on Small Satellites*, vol. 1, pp. 1–5, 1998.
- [13] G. Davidson and R. Bamler, "Multiresolution phase unwrapping for sar interferometry," *Geoscience and Remote Sensing, IEEE Transactions on*, vol. 37, no. 1, pp. 163–174, Jan 1999.
- [14] D. R. Fatland and C. S. Lingle, "Analysis of the 1993-95 bering glacier (alaska) surge using differential sar interferometry," *Journal of Glaciology*, vol. 44, no. 148, p. 532, 1998.
- [15] H. Fiedler, G. Krieger, F. Jochim, M. Kirschner, and A. Moreira, "Analysis of satellite configurations for spaceborne sar interferometry," in *Proc. Int. Symp. Formation Flying Missions Technol.*, 2002.
- [16] T. Flynn, "Consistent 2-d phase unwrapping guided by a quality map," in *Geoscience and Remote Sensing Symposium, 1996. IGARSS '96. 'Remote Sensing for a Sustainable Future.'*, *International*, vol. 4, May 1996, pp. 2057–2059 vol.4.
- [17] A. K. Gabriel and R. M. Goldstein, "Crossed orbit interferometry: Theory and experimental results from sir-b," *Int. J. Remote Sensing*, vol. 9, no. 8, pp. 857–872, 1988.
- [18] F. Gatelli, A. M. Guarnieri, F. Parizzi, P. Pasquali, C. Prati, and F. Rocca, "The wavenumber shift in sar interferometry," *IEEE Transactions on Geoscience and Remote Sensing*, vol. 32, no. 4, p. 855, 1994.
- [19] R. Gens and J. L. Vangenderen, "Sar interferometry: Issues, techniques, applications," *International Journal of Remote Sensing*, vol. 17, pp. 1803–1835, 1996.
- [20] D. Geudtner, "Die interferometrische verarbeitung von sar-daten des ers-1," Ph.D. dissertation, DLR-Forschungsbericht 95-28, 1995.
- [21] D. C. Ghiglia and L. A. Romero, "Robust two-dimensional weighted and unweighted phase unwrapping that uses fast transforms and iterative methods," *J. Opt. Soc. Am. A*, vol. 11, no. 1, pp. 107–117, 1994.
- [22] S. Gidlund, "Design study for a formation-flying nanosatellite cluster," Ph.D. dissertation, Lulea University of Technology, 2005.
- [23] R. M. Goldstein, H. A. Zebker, and C. L. Werner, "Satellite radar interferometry: Two-dimensional phase unwrapping," *Radio Sci.*, vol. 23, no. 4, pp. 713–720, 1988.
- [24] J. Griffith, L. Singh, and J. How, "Optimal microsatellite cluster design for space-based tracking missions," in *AIAA Guidance, Navigation and Control Conference and Exhibit*. American Institute of Aeronautics and Astronautics, 2007.
- [25] R. Hanssen, "Atmospheric heterogeneities in ers tandem sar interferometry," in *DEOS Report No 98.1*. Delft, The Netherlands: Delft University Press, 1998.
- [26] R. F. Hanssen, T. M. Weckwerth, H. A. Zebker, and R. Klees, "High-resolution water vapor mapping from interferometric radar measurements," *Science*, vol. 283, no. 5406, pp. 1297–1299, Feb 1999.

- [27] P. Hartl, "Application of interferometric sar-data of the ers-1-mission for high resolution topographic terrain mapping," *Geo-Information-Systeme*, vol. 4, no. 2, pp. 8–14, 1991.
- [28] P. Hartl and K.-H. Thiel, "Bestimmung von topographischen feinstrukturen mit interferometrischem ers-1-sar," *Zeitschrift fur Photogrammetrie und Fernerkundung*, vol. 3, pp. 108–114, 1993.
- [29] F. M. Henderson and A. J. Lewis, Eds., *Principles and Applications of Imaging Radar*, 3rd ed., ser. Manual of Remote Sensing. Wiley, 1998, vol. 2.
- [30] A. Ivanov, M.-X. He, and M.-Q. Fang, "Oil spill detection with the radarsat sar in the waters of the yellow and east china sea: A case study."
- [31] C. Jie, "Study on the key technologies of satellite-ground integration analysis for synthetic aperture radar systems," Ph.D. dissertation, Beijing University of Aeronautics and Astronautics, Beijing, China, Jan 2002.
- [32] W. Keydel, "Introduction: Background, goal and content of the lecture series on polarimetric sar interferometry," in *Radar Polarimetry and Interferometry*. RTO/NATO, 2005, ch. 1.
- [33] A. Khatri, K. Loh, M. Magnin, D. Santhanakrishnan, H. Leong, L. Teng, S. S. A., C. Gan, K. Kong, B. Ng, S. Wah, and D. Thunnissen, "Ship tracking & environmental protection satellite (steps) final report," School of Mechanical & Aerospace Engineering, Nanyang Technological University, Singapore, Oct 2006.
- [34] G. Krieger, H. Fiedler, J. Mittermayer, K. Papathanassiou, and A. Moreira, "Analysis of multistatic configurations for spaceborne sar interferometry," *IEEE Proceedings Radar, Sonar and Navigation*, vol. 150, no. 3, p. 87, 2003.
- [35] L. Laixing, "Formation flying of small satellites and its orbital configurations," *Chinese Space Science and Technology*, vol. 21, no. 1, pp. 23–28, 2001.
- [36] W. J. Larson and J. R. Wertz, Eds., *Space Mission Analysis and Design*, 3rd ed., ser. Space Technology Library. Microcosm Press, 1999, vol. 8.
- [37] L. Lin, *Orbit Theory of Spacecraft*. Beijing: Publishing Company of National Defense Industry, 2000.
- [38] G. Margarit and J. J. Mallorqui, "Assessment of polarimetric sar interferometry for improving ship classification based on simulated data," *Sensors*, vol. 8, no. 12, pp. 7715–7735, 2008. [Online]. Available: <http://www.mdpi.com/1424-8220/8/12/7715>
- [39] M. Martin, P. Klupar, S. Kilberg, and J. Winter, "Techsat 21 and revolutionizing space missions using microsattelites," in *Proceedings of the 15th American Institute of Aeronautics and Astronautics Conference on Small Satellites*, 2001.
- [40] M. Martin and M. Stallard, "Distributed satellite missions and technologies: the techsat 21 program," in *Proceedings of the AIAA Space Technology Conference and Exposition*. American Institute of Aeronautics and Astronautics, Sep 1999.

- [41] D. Massonnet, “Capabilities and limitations of the interferometric cartwheel,” *Geoscience and Remote Sensing, IEEE Transactions on*, vol. 39, no. 3, pp. 506–520, Mar 2001.
- [42] —, “Roue interferometrique,” French Patent 236 910D17 306RS, 1998.
- [43] D. Massonnet, E. Thouvenot, S. Ramongassie, and L. Phalippou, “A wheel of passive radar microsats for upgrading existing sar projects,” in *Geoscience and Remote Sensing Symposium, 2000. Proceedings. IGARSS 2000. IEEE 2000 International*, vol. 3, 2000, pp. 1000–1003 vol.3.
- [44] D. Massonnet and J.-C. Souyris, *Imaging with Synthetic Aperture Radar*, ser. Engineering Sciences: Electrical Engineering. EFPL Press, 2008.
- [45] E. H. Peterson, “Applications and orbit scenarios for a multistatic insar formation flying microsatellite mission,” Master thesis, University of Toronto, 2008.
- [46] E. Pottier, J.-S. Lee, and L. Ferro-Famil, “Advanced concepts in polarimetry,” in *Radar Polarimetry and Interferometry*, ser. RTO Educational Notes. RTO/NATO, 2005, ch. 4-5.
- [47] S. Ramongassie, L. Phalippou, E. Thouvenot, and D. Massonnet, “Preliminary design of the payload for the interferometric cartwheel,” in *Geoscience and Remote Sensing Symposium, 2000. Proceedings. IGARSS 2000. IEEE 2000 International*, vol. 3, 2000, pp. 1004–1006 vol.3.
- [48] R. Raney, “Radar fundamentals: Technical perspective,” in *Principles and Applications of Imaging Radar*, 3rd ed., ser. Manual of Remote Sensing, F. M. Henderson and A. J. Lewis, Eds. Wiley, 1998, vol. 2.
- [49] Z. Running, L. Yang, and L. Shengli, “System requirements and mission analysis for spaceborne sar,” in *The International Archives of the Photogrammetry, Remote Sensing and Spatial Information Sciences*, 2008.
- [50] C. Sabol, R. Burns, and C. A. McLaughlin, “Formation flying design and evolution,” in *Proc. of the AAS/AIAA Space Flight Mechanics Meeting*, 1999.
- [51] R. Sedwick, E. Kong, and D. Miller, “Exploiting orbital dynamics and micropropulsion for aperture synthesis using distributed satellite systems: Applications to techsat 21,” *Proceeding of the AIAA Defense and Civil Space Programs Conference and Exhibit, Huntsville, AL, Oct. 28-30 1998*, 1998.
- [52] S. Suchandt, M. Eineder, H. Breit, and H. Runge, “Analysis of ground moving objects using srtm/x-sar data,” *ISPRS Journal of Photogrammetry & Remote Sensing*, vol. 61, pp. 209–224, 2006.
- [53] H. Zebker, T. Farr, R. Salazar, and T. Dixon, “Mapping the world’s topography using radar interferometry: the topsat mission,” *Proceedings of the IEEE*, vol. 82, no. 12, pp. 1774–1786, Dec 1994.